Multiscale land-atmospheric feedbacks intensify hot droughts over global river-basins

Somnath Mondal
Postdoctoral Research Fellow

Auroop R. Ganguly
Professor, Northeastern University

For correspondence, please contact:
somnathpapai@gmail.com, auroop@gmail.com

This paper is a non-peer-reviewed preprint submitted to EarthArXiv.

Abstract

When drought and heatwave coincide as hot drought, its impacts exceed the sum of individual hazard. The understanding that hot drought intensifies through soil drying is incomplete. We instead find amplification and suppression of hot droughts over both dry and wet soils, with wet (dry) soil associated amplification (suppression) being the secondary pathway. Moreover, soil-moisture control on land–atmospheric coupling is scale-dependent. So, we hypothesize that hot drought severity reflects not only regional mean land-atmospheric feedbacks but also the spatial coherence of drying within and (propagation) across a region. These three-nested hypothesis explains up to 32% of hot drought severity across 30 major river basins over 1980–2023. At the basin scale, hot droughts over subtropics have come to intensify more through soil moisture associated warming than precipitation deficits, except in eastern Asia. Within basins, the spatial coherence of soil drying explains up to 12% of hot-drought severity and this contribution strengthens with drying itself in one-third of basin segments. Contrasting moisture deficit and heat propagation amplify hot droughts over basins in southwest USA and monsoon-influenced Asia, respectively. These show mean feedback, intra-basin coherence of soil moisture, inter-basin propagation as first-order and nonstationary controls of hot drought severity, with implications for regional risk estimation under warming.

Main

The concurrence of droughts[1–4] and heatwaves[5–7], hot droughts (HD)[8–10] cause disproportionate damage[8,8,10–19] more than the sum of the individual extremes. HDs start with circulation anomalies[20–22] but their regional severity is largely moderated by land–atmospheric (LA) feedbacks, where soil moisture (SM) plays a central role[23–26]. The established understanding (Figure 1a) is that dry soil intensifies hot droughts through negative coupling[27,28] between SM and daily maximum temperature (T_{max}). This coupling can act in two pathways[27]. (1) Downward: elevated $T_{\max}$ raises evaporation E (positive $T_{\max}$–E coupling) and depletes SM (negative E–SM coupling). (2) Upward: SM depletion pushes the soil into a water-limited regime where SM controls E (positive SM–E coupling), partitioning net incoming radiation toward sensible heat (negative E–$T_{\max}$ coupling). Under observed warming, widespread decline of SM reduces the evaporative fraction, shifting the LA feedback toward the upward coupling[27], whereby SM becomes the first-order control on hot drought severity. Notwithstanding, this understanding is, however, incomplete.

Positive SM–$T_{\max}$ coupling arises in regions such as monsoons[29], irrigated croplands[30,31] where wet soil induced vapor-driven longwave trapping overwhelms evaporative cooling(Figure 1b), concentrating summer heat and humidity[32] in shallow boundary layer[31–33]. Soil moisture variations can also amplify hot drought through precipitation (P) deficits where $SM - P$ coupling is scale dependent. At the mesoscale, dry soil[34] can influence convection (negative $SM - P$ coupling), whereas at continental scales precipitation[35,36] tracks evaporation (positive $SM - P$ coupling). The observed decline in soil moisture is expected to strengthen LA coupling[23,25], raising the stakes for correctly attributing hot-drought severity to SM. We therefore develop a diagnostic that (i) quantifies the modulation of SM and HD severity covariation directly from observations and (ii) decomposes it into thermal and hydrological components.

Beyond the mean regional SM state, trends in soil moisture may also reorganize its spatial structure (Figure 1c) since spatial standard deviation of SM is an upward-convex, non-monotonic function of the spatial mean from regional to continental scales[37–39]. This is critical since a region with coherent soil moisture deficit[40] is likely to have amplified hot drought severity whereas patchy deficit would suppress hot drought through thermal and moisture geadients[41]. Furthermore, 40% of summer land precipitation is sourced from upwind land evaporation[36], and precipitation is a first-order thermal regulator during summer[8], drying in one basin can propagate (Figure 1d) depleted moisture and elevated heat into neighbours[42,43]. This is critical since widespread synchronous drying can produce heating anomalies large enough to stabilize the driving blocking circulation[44].

We test these three multi-scale SM controls on HD severity across 30 major river basins, each partitioned into upper, middle, and lower segments (81 segments in total) over 1980–2023 (Methods). We choose river basins since they are coherent hydrological unit and concentrate population, socio-economic activities, and are the standard management unit for water resources and hazard monitoring worldwide (GWP–INBO, 2009; UN-Water, 2021). The complete framework address five core research questions: (1) How does SM covary with hot drought, through what mechanistic pathways, and whether it varies regionally or temporally? (2) Has the sensitivity of HD severity to SM intensified across major river basins and does this intensification is more associated with dry or wet soil and the corresponding pathways? (3) Does the spatial coherence of soil-moisture deficits within a basin modulate hot drought severity (4) Does propagation over cross-basin pathway modulate hot drought severity? (5) What fraction of HD severity is jointly explained by these three mechanisms: regional feedback, spatial clustering, and cross-basin propagation and where is this intensifying most rapidly?

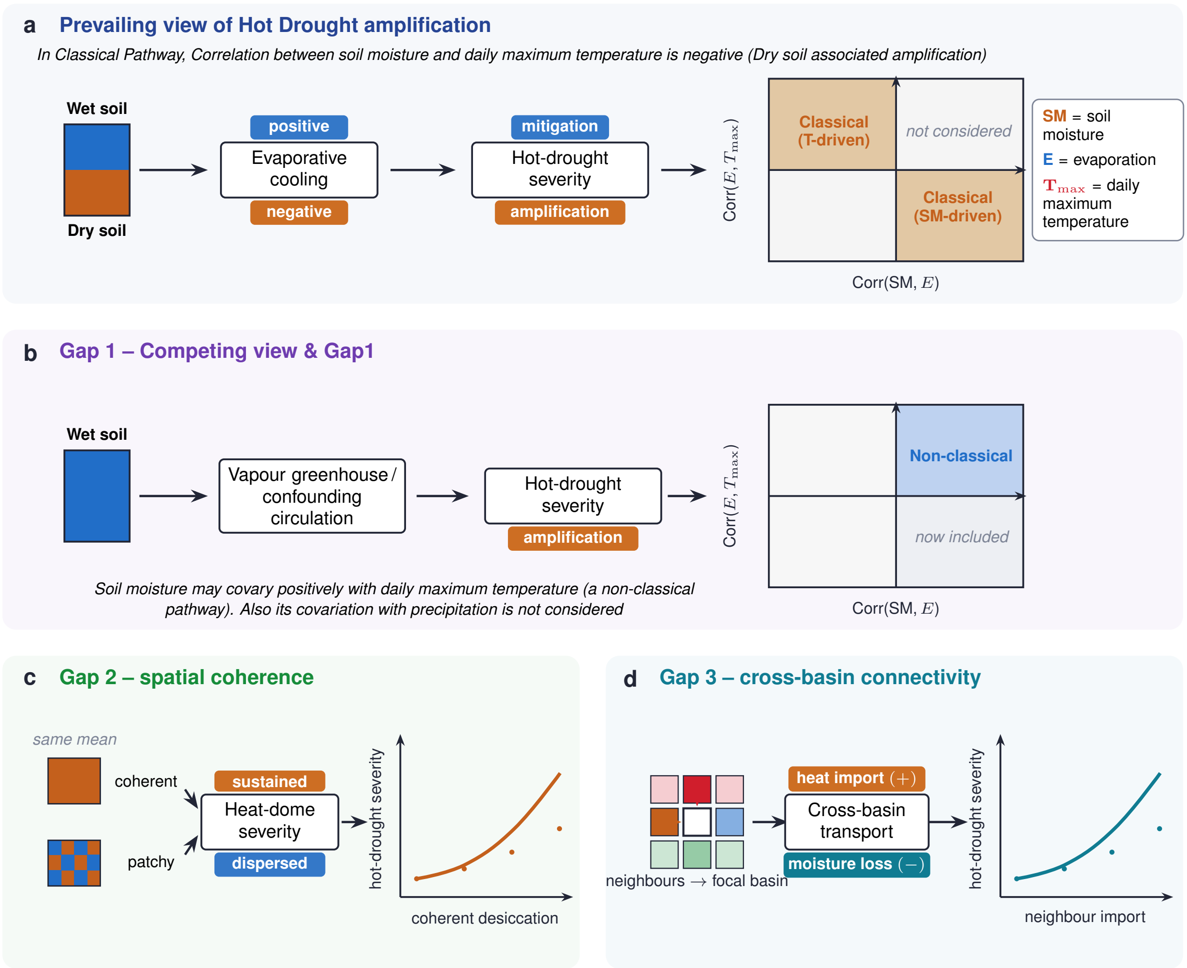

Figure 1: | **Hypothesizing multi-scale control of Soil Moisture on Hot droughts**. (a) Classical coupling during hot drought where depleted soil moisture (via evaporation) leads to more warming (negative correlation between soil moisture and daily maximum temperature). (b) non-classical coupling where soil moisture is positively correlated with daily maximum temperature. Also the contemporary studies completely ignores the the feedback of soil moisture on the local precipitation via evaporation or dynamic influences. (c) Spatial organization of soil moisture deficits and (d) propagation from and to neighboring regions can influence regional hot drought severity

Dynamic Soil moisture–hot drought covariations and its land–atmospheric pathways

We use soil-hot drought covariation to associates daily HD severity to the soil moisture anomalies (SM') while conditioning on 500-mb geopotential height (Z'_{500}) anomalies (Methods; equations 2). For each grid cell and each year, δ_1 and δ_2 represents sensitivity of daily HD severity to soil moisture (SM') and 500-mb geopotential height (Z'_{500}) anomalies, respectively. Similarly we use Conditioned Mediated sensitivity (CMFS) framework (Methods; equations 4-6) to decompose the LA pathway $\mathrm{SM}' \to E' \to \{T'_{\max}, P'\}$ while controlling for Z'_{500} at each stage. We quantify the sensitivity of evaporation to soil moisture ($\hat{\alpha}_1$), which in turn can influence T'_{max} ($\hat{\gamma}_1$), P' ($\hat{\phi}_1$). The mediated sensitivity composites $\hat{\alpha}_1\hat{\gamma}_1$ and $\hat{\alpha}_1\hat{\phi}_1$ are therefore the indirect effects of SM' on $T'_{\max}$ and P', respectively, routed through E'. This products are referred to as CMFS_T and CMFS_P, respectively.

The sign of δ_1, CMFS_T and CMFS_P encodes the prevailing $SM - HD$ coupling and the corresponding LA pathways. For instance, a negative (positive) δ_1 indicates that, on average, the land surface's will experience amplified hot drought severity if it is abnormally dry (wet). Similarly, a negative (positive) value of CMFS_T (CMFS_P) indicates dry soil is associated with warming and drying whereas a positive (negative) means either LA is decoupled from soil moisture or where its driven by external forces (i.e.- vapor heat trapping, circulation).

Here, note that δ_1, CMFS_T and CMFS_P is an average summer sensitivity. To quantify the cumuliative SM contribution over each summer to hot drought severity, warming and drying, we employ C_{SM}, $C_{\mathrm{SM},T}$, $C_{\mathrm{SM},T}$ defined as cumuliative sum of the sensitivity coefficients with SM' over all active hot-drought days (Methods: equations 3, 7). Because the contribution is the sensitivity times SM', its sign relative to the sensitivity reveals the sign of cumulative SM'. Therefore, using joint sign of δ_1 and C_{SM}, we define 4 mutually exclusive $SM - HD$ coupling regimes: drying-associated amplification (**DA**; $\delta_1 < 0$, $C_{\mathrm{SM}} > 0$) and wetting-associated amplification (**WA**; $\delta_1 > 0$, $C_{\mathrm{SM}} > 0$), soil drying associated suppression (**DS**; $\delta_1 > 0$, $C_{\mathrm{SM}} < 0$); and wetting-driven suppression (**WS**; $\delta_1 < 0$, $C_{\mathrm{SM}} < 0$).

Similarly, based on the joint signs of CMFS_T and CMFS_P, and whether the realized contributions are active ($C_{\mathrm{SM},T} > 0 : warming, C_{\mathrm{SM},P} < 0 : precipitationsuppression$) or structural (wetting and/or cooling) on the active hot-drought days, each grid cell is assigned to one of twelve mutually exclusive categories (Methods; Table 2). We define $\mathrm{CMFS}_T < 0$, $\mathrm{CMFS}_P > 0$ as classical coupling/regime where dry soil drives warming and precipitation suppression, yielding three categories depending on whether warming and drying is equal (C_{TP}) or one dominates (C_T, C_P). The C_X is where wet anomalies mute the warming and/or drying feedbacks. We define $\mathrm{CMFS}_T > 0$, $\mathrm{CMFS}_P < 0$ as non-classical regime where wet soil is associated with warming and precipitation suppression giving the analogous N_{TP}, N_T, N_P. N_X is non-classical counterpart of C_X. $T1$ ($P1$) represent single pathway thermal (hydrological) based warming (drought) whereas $T2/P2$ represent similar pathway but doesn't produce warming or cooling.

Figure 2 shows the $SM' - HD$ coupling regimes over Southwestern North America

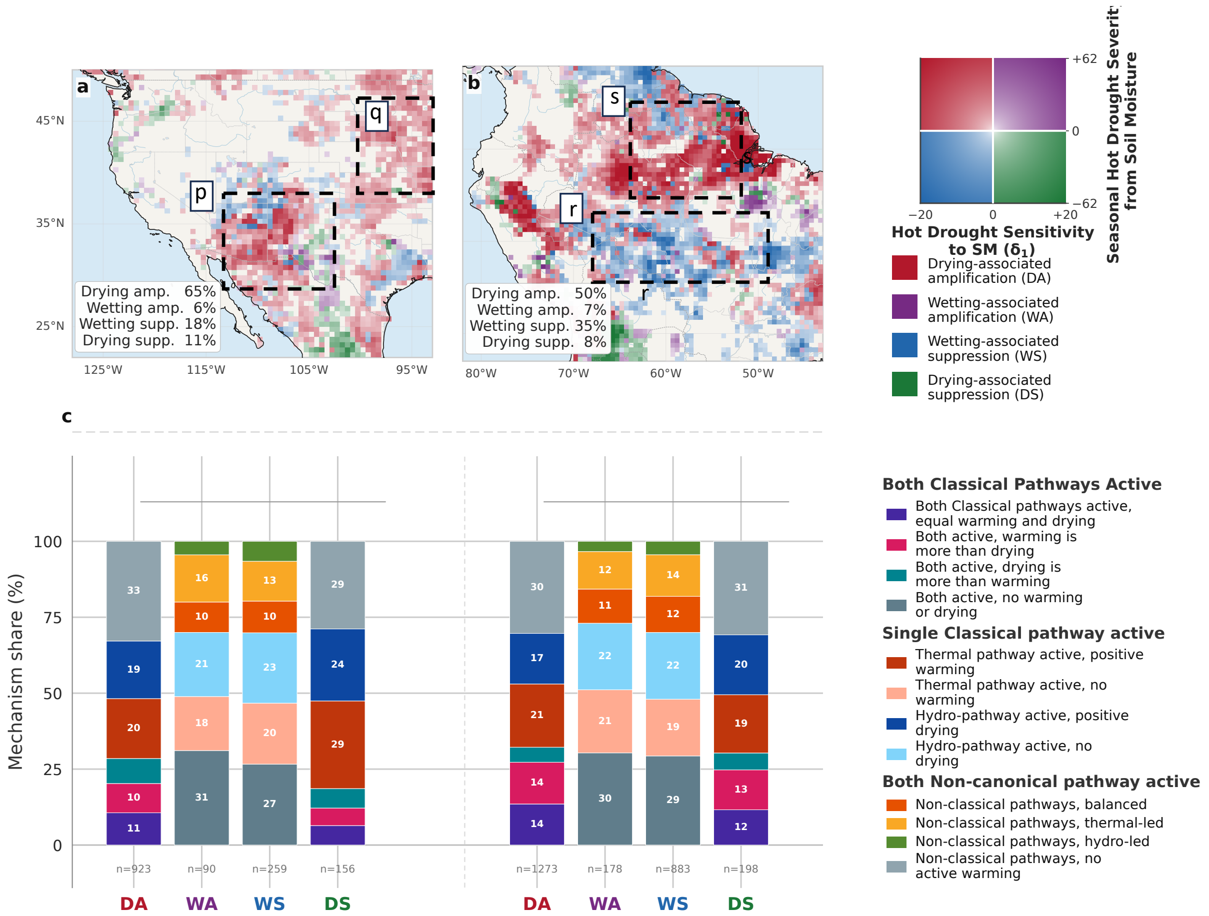

Figure 2: | **Soils moisture amplify hot drought severity through thermal and/or hydrological feedbacks.** Where and how strongly soil moisture is associated with hot drought severity in south-western North America (a) and the Amazon (b) in 2023 summer.Each grid cell is coloured by two quantities simultaneously: δ_1 and C_{SM}. Red (blue) tones indicate that dry (wet) soil is associated heat extremes. Color saturation reflects signal strength.(c,d) For each coupling regime identified in panels (a,b), the bars show what heterogenity in land-atmospheric feedback pathway of grid cells experienced. Classical and single thermal or hydrological coupling events (purple) dominate the drying associated amplification quadrants in both regions, whereas suppression and non-classical coupling are more common where coupling is associated with wet soil.

(SWNA) and over Amazon during boreal summer 2023 when both regions were severely impacted by HDs[8,45]. Over SWNA, DA regime is concentrated over northwestern Mexico, 4-corner states in USA (Box p, Figure 2) consistent with a amplified regional hot drought severity due to suppressed North American monsoon combined with dry soils over Mexico[8]. Elevated severity also extends to the Northern Great Plains (Box q, Figure 2). Over South America, DA regimes encompass the entire Amazon basin (Box s, Figure 2). whereas elevated terrain and mixed irrigation (Box r, Figure 2) regions exhibit WS regime. WA regimes are present but only at 6% and 5%. Nearly 30-40% of grid locations across both regions are DS and WS. Notably, suppression-regime grid cells may still experience elevated HD severity as observed over SWNA (Supplementary Figure 1) through the influence of Z'_{500} anomalies.

Figure 2 (panel c) presents the percentage contribution of each LA pathways within each bivariate quadrant (DA, WA, WS, DS) for SWNA and the Amazon basin. Across both regions, the DA exhibits the highest fractional occurrence of classical compounding and single pathway feedback (T1, P1, C_{TP}, C_T, C_P: $\sim$67%), providing a direct mechanistic basis for HD amplification: concurrent soil moisture deficits reinforce surface warming and drought through the land–atmosphere feedback pathway. However, N_X category within DA ($\sim$31%), indicates that a substantial fraction of DA cells have non-classical evaporative wiring where the net severity amplification operates beyond the evaporation-mediated thermal and hydrological pathways. In contrast, the wetting regimes (WA and WS) are dominated by structural categories (C_X: $\sim$30%; T2: $\sim$19%; P2: $\sim$22%) as well as non-classical compound categories (N_{TP} + N_T: $\sim$27–30%). We repeated this analysis for SWNA and the Amazon in 2010 (Supplementary Figure 2), and for Central Europe, East Asia, and the globe in 2022 (Supplementary Figures 3-4). Although DA extent varied across regions and years, the relative shares of classical and non-classical feedback categories within the drying- and wetting-associated HD regimes stayed the same—suggesting this LA pathway architecture is an intrinsic feature of how HD severity covaries with dry or wet soil.

Amplifying soil drying associated hot droughts Over river Basins

We compute δ_1 and $f_{\mathrm{SM}} = C_{\mathrm{SM}}/\hat{C}_y$ (Methods) for 81 segment–year combinations over 1980–2023, and present the $SM - HD$ and LA (CMFS) coefficients for Amazon (Lower: L), Colorado (Middle:M), Murray–Darling (Upper:U), and Zambezi (L) (Figure 3). Results for all remaining segments appear in the Supplementary Figures 5-24. Here we examine the individual pathway coefficients α_1, γ_1, and ϕ_1 since a trend in CMFS_T may reflect weakening α_1, strengthening γ_1, or both, distinctions obscured by the product term. Across all 81 segments, δ_1 exhibits the characteristic spike behavior (Figure 3), with 18 segments showing significant monotonic trends. The dominant trend is negative concentrated in the semi-arid Americas, tropical South America, and temperate Europe along with an increasing frequency of DA regimes. Significant positive trends, are confined to Zamebji and Amur segments. An intensifying negative (positive) trend corresponds to greater hot drought severity for the same negative (positive) SM', implying regional intensification of hot droughts. Consistent with δ_1, the LA-pathway coefficients α_1, γ_1, and ϕ_1 exhibit inter-annual variability, implying that these feedbacks activate preferentially in specific years rather than operating as a uniform background process.

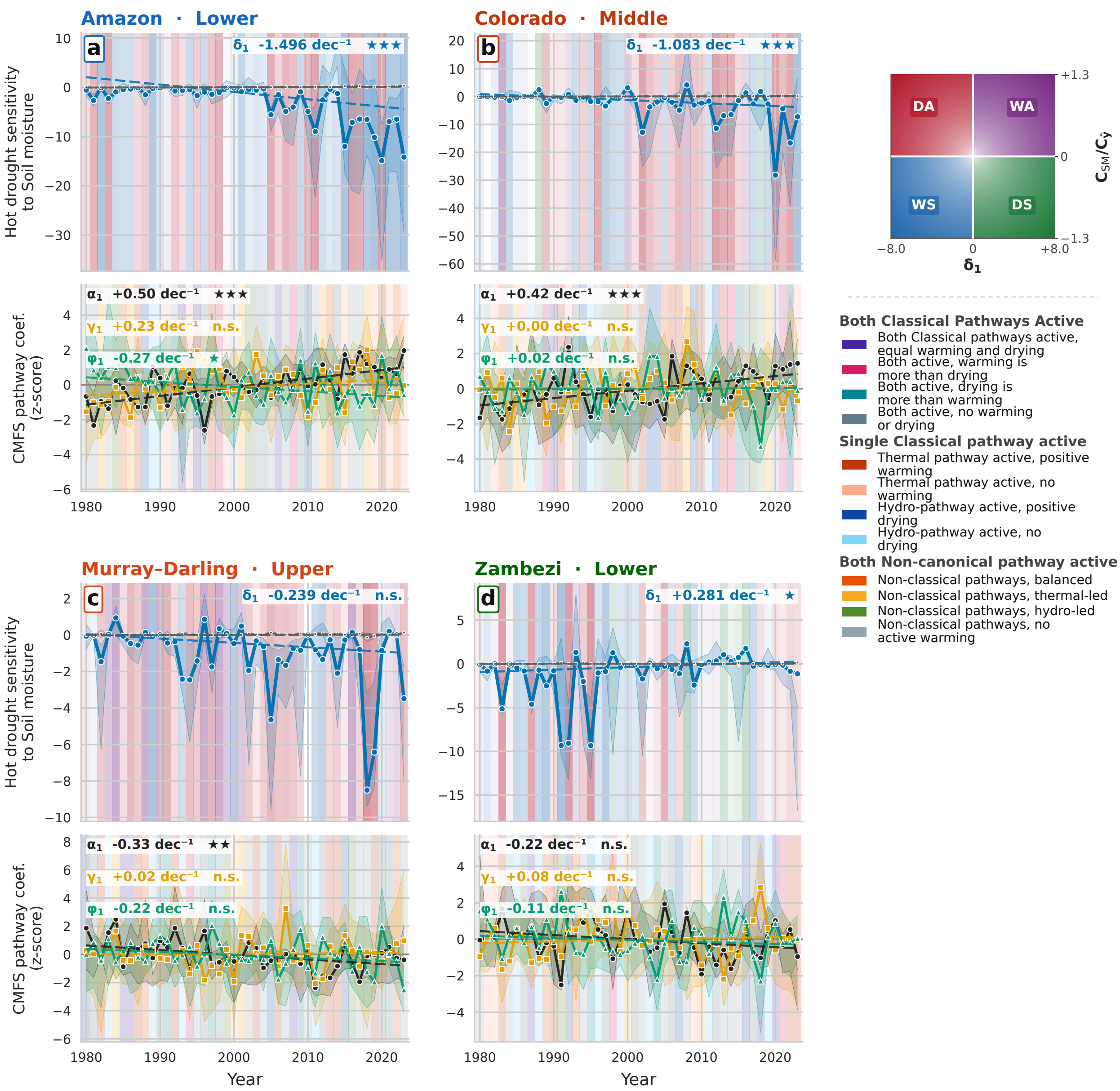

Figure 3: | **Intensifying soil moisture and hot drought covariation across major river basins** (a–d) time series of soil-moisture-hot drought and land-atmospheric (CMFS) coupling coefficients for four river basin segments: Amazon Lower (a), Colorado Middle (b), Murray–Darling Upper (c), and Zambezi Lower (d). Each panel pair shows two quantities.Upper sub-panel shows the sensitivity of hot drought severity to SM′ (δ_1, blue) with dashed lines showing Theil–Sen trends; background colour encodes the soil-hot drought coupling regime in each year. Lower sub-panel shows z-scored land–atmosphere pathway coefficients: sensitivity of evaporation to soil moisture (α_1), daily maximum temperature to evaporation (γ_1), and precipitation to evaporation (φ_1). Background shading indicates the LA feedback pathway in each year

Amazon (L) exhibits the strongest decline (-1.496 decade^{-1}), followed by Colorado (M) (-1.083 decade^{-1}), while Colorado (U) and Colorado (L) show significant but weaker negative trends. Within the Amazon, Amazon (M) shows a significant negative trend (-0.685 decade^{-1}, $p < 0.001$). Colorado (M) shows strong and significant trend in α_1 ($+0.4978$ decade^{-1}) with no trend in γ_1 and ϕ_1. This implies that in water-limited Colorado (M), soil's strengthening control over E', but this does not translate to further warming or precipitation suppression. However, over Rio-Grande (U), upward coupling is strengthening in atmospheric feedback pathways ($t(\delta_1) = -0.765$, $t(\alpha_1) = +0.367$ where t is the decadal trend) along with ϕ_1 trends implies that the entire land-atmosphere cascade from SM$-$E through E$-$P is being activated simultaneously. Amazon (L) exhibit increased control of soil moisture on evaporation ($t(\alpha_1) = +0.418$) although the underlying trends in LA coefficients differ($t(\gamma_1) = +0.2277$, $t(\phi_1) = +0.2686$). Note that positive trends in both α_1 and γ_1 do not imply the two are simultaneously positive. They follow different modes of variability and so more regimes may show either upward ($\alpha_1 > 0$) or downward ($\gamma_1 > 0$) coupling. If both are positive, HD severity is amplified through circulation in which SM$'$ and E' covary (non-classical coupling). However, the ϕ_1 shows significant negative trend suggesting contrasting activation and deactivation of thermal and hydrological arm of LA pathways over Amazon (L). Intensification of upward coupling similar to Colorado (M) is also detectable across Colorado (U & L), Congo middle, Nile Upper,Rhine middle,and Tigris & Euphrates lower.Coupling similar to Amazon (L) is also observed in Sao Francisco upper, Orinoco middle, Danube middle and Volga lower.

Over Murray Darling (U), α_1 exhibits a significant decreasing trend (-0.332 decade^{-1}) suggesting progressive decoupling of soil moisture from evapotranspiration. Since this decoupling coexists with a weakly significant but strong negative δ_1 trend, the $SM-HD$ interactions is likely driven by factors other than LA feedbacks (i.e.- shifts in the regional hydroclimatic mean state). This configuration of $SM' - E'$ decoupling alongside stable or intensifying δ_1 constitutes a geographically coherent signal of demand-side forcing (upward coupling) that reappears across the South Asian monsoon zone, most prominently in Brahmaputra Lower ($t(\delta_1) = -0.16$, $t(\alpha_1) = -0.342$), Ganges Lower, and Yangtze Lower and Middle, pointing to a transition across the monsoon-influenced basins of South and East Asia. Both Zambezi (Lower) and Amur (Lower) exhibit statistically significant positive δ_1 trends (Zambezi: $+0.281$ decade^{-1}; Amur: $+0.272$ decade^{-1}), a wetting associated hot drought amplification contrary to the widespread drying elsewhere. At both basins, α_1 trends negative indicating progressive decoupling.

The changes in 12-category CMFS distributions reveal period-to-period (Supplementary Figures 25-26) structural reorganisations. The most widespread is active thermal activation: T1 rising by 9–23% is detectable across climate zones from the Colorado to the Rhine, Yellow, Volga, and Niger Middle and the monsoon zones such as Ganges (L) and Brahmaputra (L). Colorado (M) exhibits shift, from structurally passive categories (N_X: 18%; T2, P2, C_X: 14% each) to co-dominant T1 and P1 (23% each, +18 pp); within DA years, N_X collapses from 43% to near-zero as T1 and P1 each rise to 36%, a transition consistent with the observed strengthening of upward coupling. Amazon (M) shows a contrasting shift. Within DA years N_X rises from 25% to

36% as P1 declines and T1 emerges (21%) validating deactivation (activation) of (hydrological) thermal feedbacks. The second tendency is N_X expansion as the signature of SM–E decoupling. For instance in Murray–Darling (U) within DA years, the early dominance of T1, C_{TP}, and C_P shifts to N_X and T1, a pattern shared by Indus Lower (+32%) and Irrawaddy Middle (+27%). Third tendency is the reorganization of dual (C_{TP}, C_T, C_P) to single LA pathways ($T1$, $P1$) with regional and pathway variations. For instance, Yangtze Lower (C_{TP}: -23%, $P1$: $+27\%$) shows intensifying hydrological feedback where as Mekong Middle and Upper show thermal dominance (significant positive γ_1 trends).

Spatially coherent drying amplifies hot drought severity

The $SM' - HD$ interaction framework leaves a substantial fraction of the severity amplification unexplained. Furthermore, median residuals from the $SM' - HD$ interaction framework show strong correlation with spatial autorcorrelation structure (median Moran's Index, I_{SM}) of SM$'$ in the basin segments (supplementary figure 27, Methods). Therefore, we hypothesize that a basin where a negative SM$'$ anomaly is spatially coherent is expected to show a much stronger response and hence a larger, systematically explainable residual than one where an anomaly of similar regional mean is patchy and disorganized.

Here we develop a spatial clustering moderation framework (Methods; equations 8 and 9) across 30 major river systems through two regression blocks: (i) a primary model with I_{SM} as covariate and (ii) a sensitivity model augmenting the primary model with clustered SM anomalies ($\hat{I}_{SM} \cdot \hat{SM'}$) for which the incremental R^2_{aug} indicates how the sensitivity model can explain hot drought severity residuals. Temporal trends in R^2_{aug} and in the desiccation clustering index $-I_{SM} \cdot SM'$, restricted to active days (Methods), are estimated via Theil–Sen slope regression and assessed with Mann–Kendall tests across the 1980–2023 record (Supplementary Figure 28). We also provide the explainability by clustering R^2_{aug} for six focus segments over 1980-2023 (Figure 4).

Thirty of 80 segments occupied the amplification quadrant (supplementary figure 27) with concurrent positive trends in both $R^2_{\text{aug,act}}$ and the $-I_{SM} \cdot SM'$. Here note that most of these trends are weak or not significant. Statistically significant ($p < 0.05$) temporal trends in $R^2_{\text{aug,act}}$ were identified in only two segments: Rio Grande Upper ($+0.01265$ dec^{-1}) and Orange Upper (-0.00878 dec^{-1}) while nine showing significant trends in the coherent drying ($-I_{SM} \cdot SM'$) itself such as Rhine Upper, Volga Lower, Congo Lower , Columbia Upper, Nile Upper, Rhine Middle, Ganges Upper, Colorado Upper, and Volga Upper. Across the six focus segments (Figure 4), the conditional Spearman correlation between the coherent drying ($-I_{\text{SM}} \cdot SM'$) and absolute residual on active days was positive and highly significant (Figure 4e-h) throughout, ranging from $\rho = +0.338$ (Zambezi Lower) to $\rho = +0.598$ (Murray–Darling Upper). Moreover, the hexbin-coloured δ_1 reveals that positive residuals are preferentially colored in negative δ_1 values prominently over Colorado (M) and Murray–Darling (U). This implies that the unresolved variance is concentrated during coherent drying phases in which negative SM' amplifies LA feedbacks beyond what the basin-mean can do. The physical character of the long-term signals, however, diverges. In Rio Grande (U) residual variance is becoming increasingly sensitive to

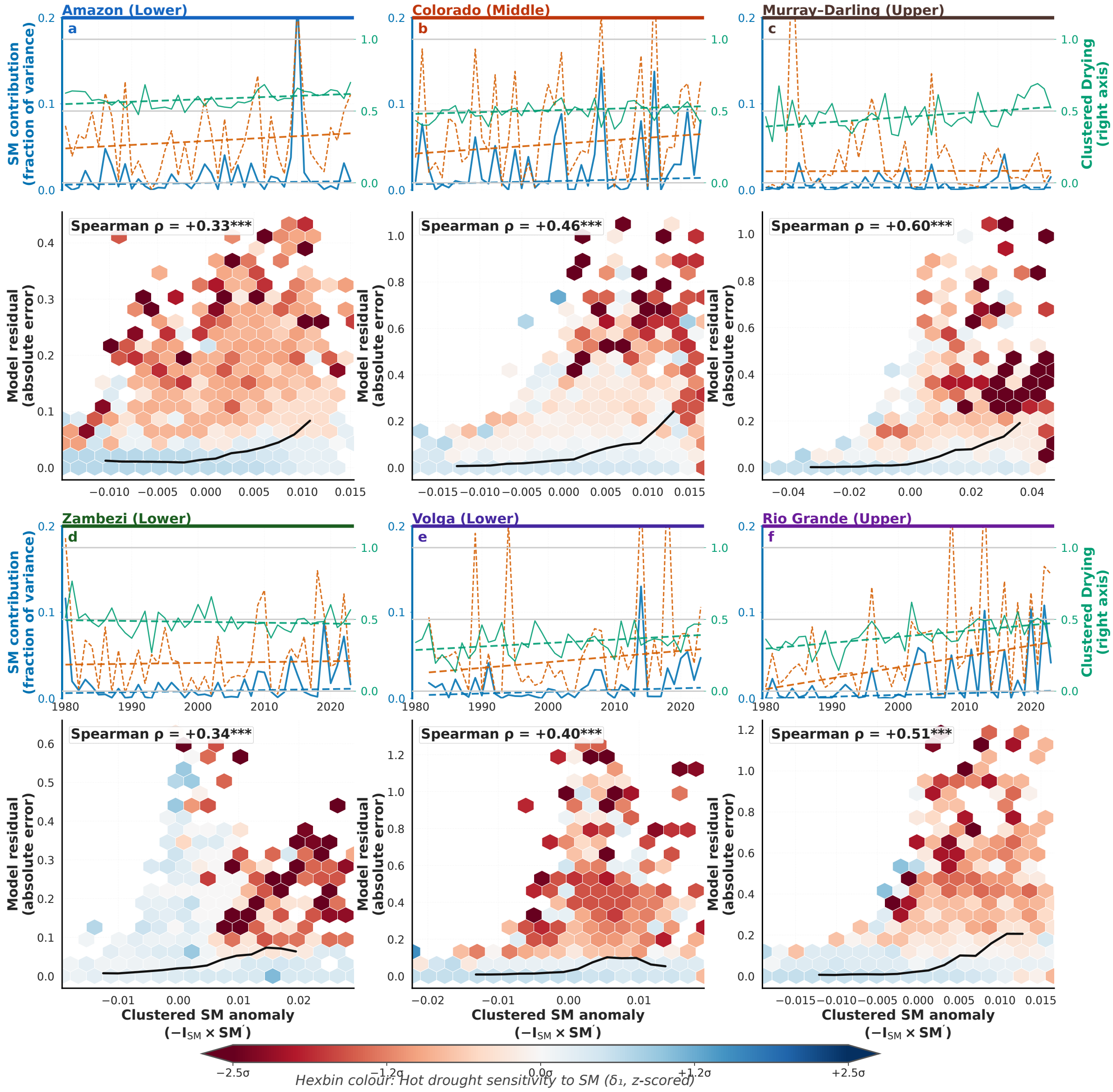

Figure 4: | **Coherent drying amplifies regional hot drought severity.** (a-f) Per-segment tripartite panels for the focus segments (river and segment labelled in each title). *Upper sub-panel*: annual R^2_{all} (blue) and $R^2_{\text{aug,act}}$ (yellow) on the left axis; summer mean mean Moran's I_{SM} (right axis, green). Dashed lines are Theil-Sen trends; *Lower sub-panel*: hexbin scatter of $I_{\text{SM}} \cdot (-\overline{\text{SM}'})$ on x-axis against the absolute residual $|\varepsilon|$ (y-axis) from soil-hot drought covariation model, restricted to active days; hexbin colour gives the per-segment z-scored δ_1.

an weakly changing I_{SM} implying increased leverage of any existing spatial organisation as the basin dries. Annual $R^2_{\mathrm{aug,act}}$ series across all segments reveal episodic extremes that transcend segment-level weak trend significance: single-year values exceed 0.20 in Tigris–Euphrates Middle (2011: 0.687), Mississippi Upper (1990: 0.508), Indus Upper (2001:0.514), Volga middle (2009: 0.418), Danube Lower (1990: 0.387), Ganges middle (2000:0.353), and Colorado Middle (2016: 0.256) confirming that clustering moderation operates as a year-to-year physical mechanism across the full sample even where no decadal trend is detectable.

Role of Remote Connectivity in Hot Drought Amplification

Here, we test whether a portion of the residual after accounting for basin-mean feedback and intra-basin spatial coherence reflects a systematic bias explainable by how the basin sits within a larger-scale setting of propagation to and from its neighbors (Table 3). Both hydrological and thermal propagations are tested simultaneously against daily neighbour-mean evaporation $\bar{\Phi}_{E'}$ and temperature anomaly, $\bar{\Psi}_{T'}$, where a priori expectations are $\lambda_E < 0$ and $\mu_T > 0$ (Methods; equations 10). This is since enhanced evaporative flux (warm air anomalies) from upstream or adjacent basins suppresses (amplify) the downwind hot drought severity. We derived the two pathway coefficients over 1980–2023 and then test whether the two pathway coefficients are themselves changing, providing a temporal dimension to the propagation signal. We also provide the time series of explainability by propagation $\Delta R^2_{\mathrm{prop}}$ for seven focus segments (supplementary figure 29).

Across the 80 river-basin segments (Figure 5a-b), propagation of both moisture and heat (classical-import) is the minority pattern ($\lambda_E < 0$, $\mu_T > 0$; $n = 19$) but significantly strong over Rio Grande (U & M) ($\lambda_E = -3.57, -2.58$), Colorado (L & M) ($\lambda_E = -1.83$, $\lambda_E = -1.54$). The heat propagation (warming import; $\lambda_E > 0$, $\mu_T > 0$) is the most populated and shows significance over Yangtze Upper and Yangtze Middle ($\mu_T = +0.011, +0.020$). Other significant warming-import corridors include Rhine Middle and Danube Upper. Under the trend classification, the moisture regime (-,-) is the most common ($n = 24$), meaning that in nearly one-third of basins sensitivity to import of moisture (or its deficit) is strengthening while 14 segments show strengthening sensitivity to both heat and moisture import.

Among the seven focus segments (supplementary figure 28) Rio Grande (U) presents the strongest moisture-import effect ($\lambda_E = -3.57$) and the significant trend ($\partial_t \lambda_E = -1.55$ dec^{-1}) and a significantly growing $\Delta R^2_{\mathrm{prop}}$ time series, reaching annual maxima of 0.13 during the drought years 2022. Colorado (M) exhibits similar pattern ($\lambda_E = -1.54$; $\partial_t \lambda_E = -0.76$ dec^{-1}; max $\Delta R^2 = 0.150$ in 2014). In contrast, Murray Darling (U) shows a comparable behavior but a significant strengthening of the warming-advection pathway. Ganges Middle displays episodic $\Delta R^2_{\mathrm{prop}}$ maxima among the focus set (0.14 in 2018, 0.12 in 2013 and 2017), despite a non-significant λ_E (+1.20) that reflects high inter-annual variance consistent with dominant monsoon system. Zambezi Lower show rather decrease in coupling with neighboring basins.

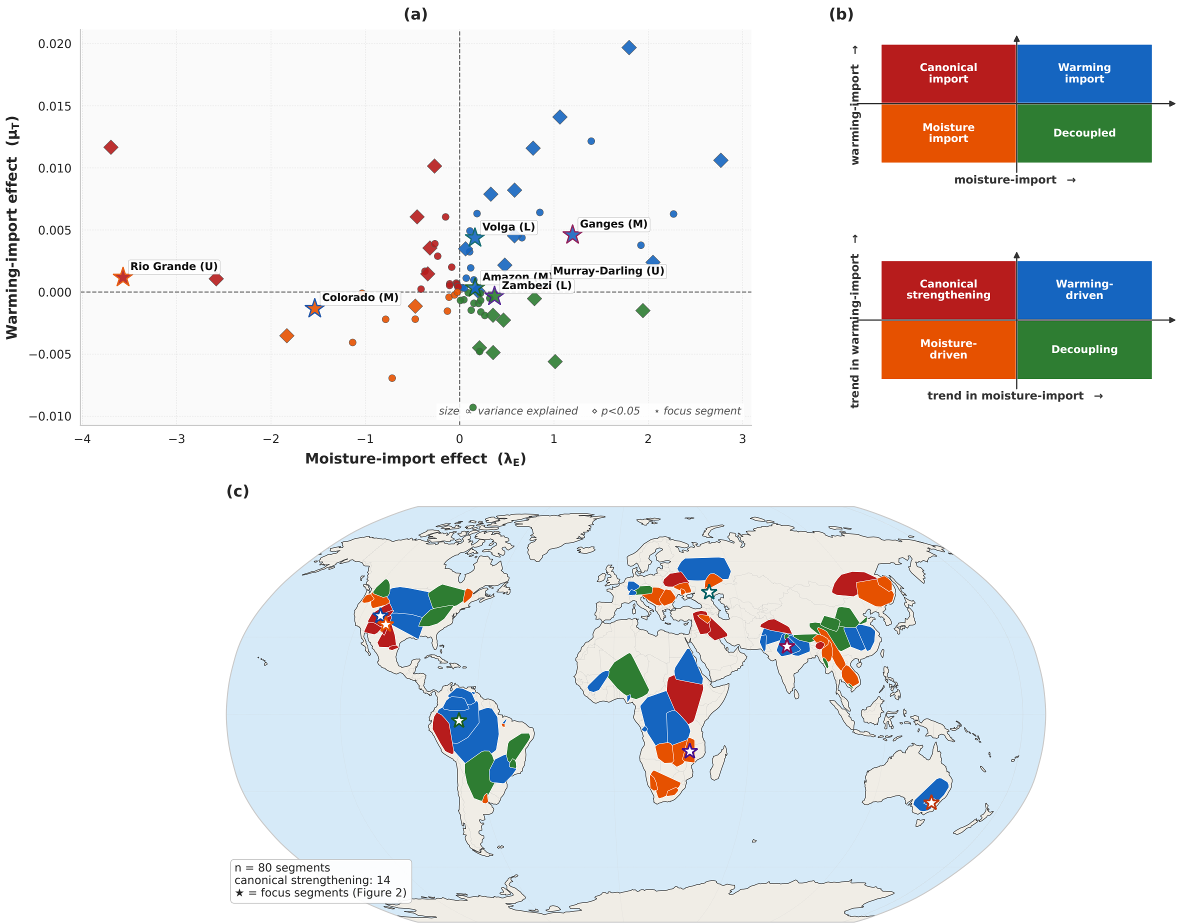

Figure 5: | **Regional Propagation modulates Hot Drought Severity.** (a) Scatter of pooled moisture-import ($\hat{\lambda}_E$, x-axis) versus warming-import ($\hat{\mu}_T$, y-axis) coefficients across all 80 segments; marker size is proportional to pooled ΔR^2_{prop}; diamonds ($\Diamond$) indicate $p < 0.05$ (HAC-robust); stars ($\star$) denote focus segments. (b) Combined colour keys for the trend-quadrant map (left) and the pooled-effect scatter (right). (c) Spatial distribution of the Theil-Sen trend bivariate quadrant for each basin segment, classifying the decadal trend in moisture-import sensitivity $\partial_t \hat{\lambda}_E$ (x-axis) against the trend in warming-import sensitivity $\partial_t \hat{\mu}_T$ (y-axis) of the neighbour-propagation model.

Explaining Hot drought severity using multi-scale land-atmospheric feedbacks

Across 30 river-basins spanning six climatic regions, we quantify the explanatory power of regional SM controls (local co-variation, spatial coherence and remote propagation) for hot-drought severity using the true total R^2_{true} (Methods; equations 11). The local basin-mean regression is the dominant contributor in every segment, consistent with basin-scale SM' thermodynamic control on regional hot drought severity. The spatial clustering provides a secondary attribution, most pronounced in monsoon and semi-arid regions of Asia and North America. The propagation reaches high mean values in Tigris–Euphrates (L), Colorado (M), Rio Grande (U). In peak drought years, the true cascade total reaches 0.3 (Amazon Lower, 2023), 0.325 (Tigris–Euphrates Lower, 2001), and > 0.28 (Colorado Middle, 2023) confirming that in extreme events the three tiers collectively account for approximately one third of the seasonal HD variance.

Of the 30 segments (Figure 6), six exhibit statistically significant positive trends in the true cascade total. Rio Grande (U) records the fastest growth ($\partial_t R^2_{\mathrm{true}} = +0.044$ dec^{-1}), supported by concurrent significant trends in basin mean feedback (+0.019 dec^{-1}), coherence (+0.013 dec^{-1}), and propagation (+0.009 dec^{-1}). Colorado (M) shows similar growth (+0.034 dec^{-1}), with significant regional mean feedback (+0.024 dec^{-1}) and propagation (+0.007 dec^{-1}) trends but a weakly-significant clustering trend. Tigris–Euphrates (L) (+0.034 dec^{-1}) and Amazon (L & M) both exhibit significant true-total growth (+0.026 dec^{-1} and +0.027 dec^{-1}), driven predominantly by basin mean feedback. Cross-regime contrasts are physically interpretable. For instance, semi-arid corridors (Colorado–Rio Grande, Tigris–Euphrates) show regional feedback and propagation strengthening together with significant or weak trend in clustering, consistent with intensifying feedbacks under sustained drying. Asian monsoon segments (Ganges Middle, Yangtze Lower) have the highest coherence means but no significant trend, consistent with the observed positive SM trend; the European group is moderate (0.159–0.197) though Rhine Middle dominates propagation in extreme years; and the African basins return the lowest totals (0.087–0.099).

Discussion & Conclusion

For decades, the amplification of hot droughts has been read through a single lens: dry soil suppresses evaporative cooling and therefore can simultaneously warm and dry the surface (classical coupling). Our results do not overturn this but demote it as one of three SM controls and the one that does not even hold universally in sign. We show that hot-drought amplification and suppression can both occur over dry or wet soil, and that the partitioning of classical and non-classical LA pathways across SM–HD coupling regimes remains invariant in time and space indicating an intrinsic property of how SM′–HD covariation translates into LA feedback pathways. Distinguishing this classical from non-classical wiring can improve compound-event forecasts. Models that assume dry soil always amplifies heat will get the severity wrong along the energy–water-limited boundary, which is shifting fastest under warming. More consequentially, activation of LA feedback across different scales is set by where a basin sits on the $SM -$

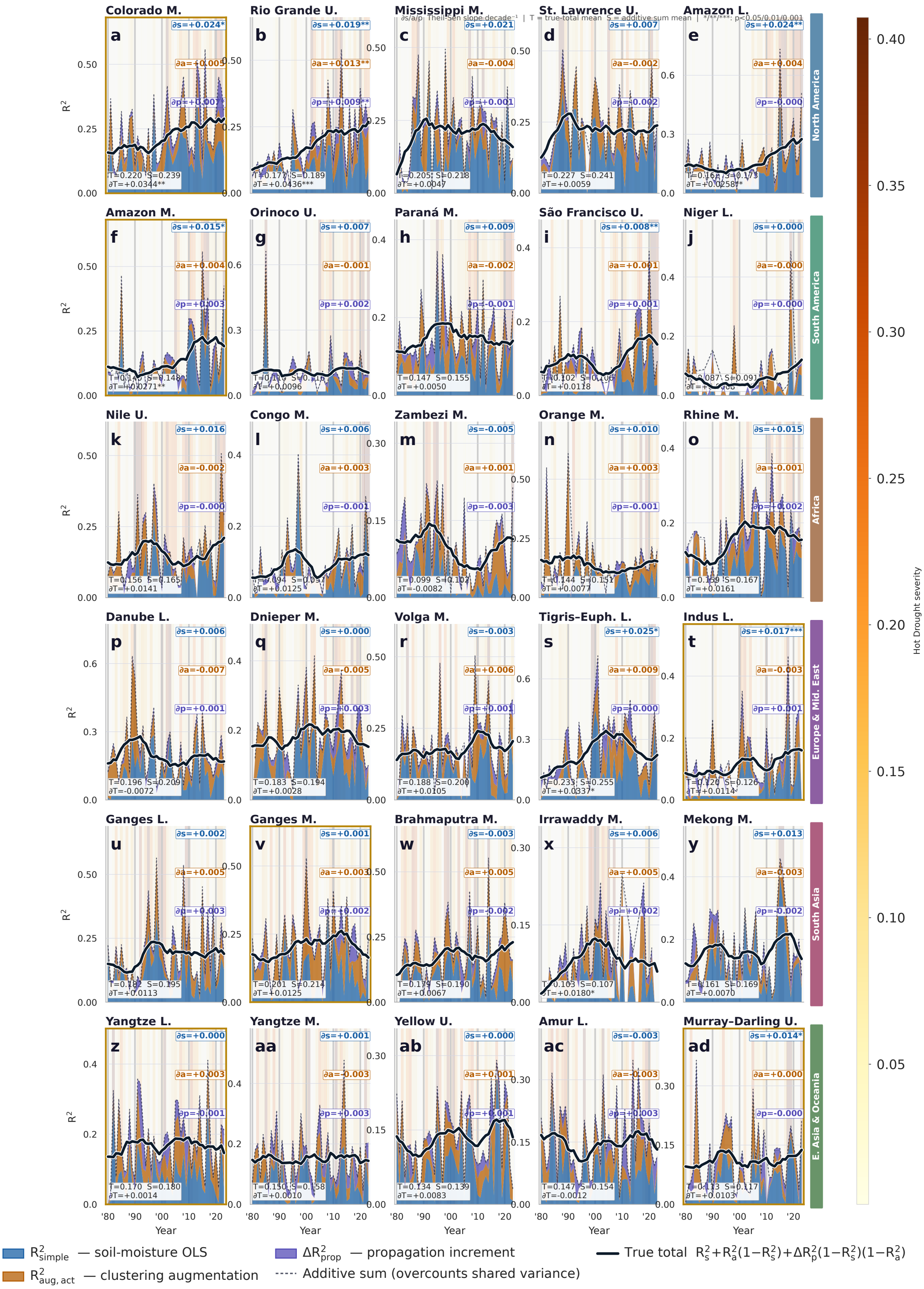

Figure 6: | **Exaplaining Hot drought severity via regional feedback, intra-region coherence and inter-region propagation across thirty basin Segments, 1980–2023.** Stacked filled areas show the explained variance contributed by: R^2_{simple} (blue; Stage 1: regional feedback), $R^2_{\text{aug,act}}$ (orange; Stage 2: intra-basin coherence), and ΔR^2_{prop} (purple; Stage 3: inter-basin propagation). The true variance total is shown as the bold dark line. Background shading encodes annual average hot drought severity. Inset annotations shows Theil-Sen trend.

HD coupling spectrum. In semi-arid corridors (Colorado–Rio Grande, Tigris–Euphrates), the regional feedback and cross-basin tiers strengthen together. In the Asian monsoon basins, the spatial-coherence of soil moisture dominates, reflecting contiguous, seasonally organised SM' that a mean-state model cannot resolve. R^2_{true} is therefore itself a diagnostic measures not just how much variance is explained, but how deeply hot droghts in region is coupled with SM across grid-point scale, through basin-mean feedback, to multi-basin (continental) connectivity.

This ordering would be of largely descriptive interest were the structure stationary. But, it is not. The regional mean feedback is intensifying with strongest signals over tropical and subtropical regions of Americas, Europe and semi-arid west Asia. The sensitivity to cross-basin moisture-import is strengthening across nearly a third of basins while it strengthen in another sixth implying increased remote-sensitivity of regional hot droughts. Because the multi-scale LA feedbacks driving hot droughts are non-stationary, hazard products built on historical climatology are already stale and the direction of that staleness varies by region rather than being uniform.

The current study has limitations. The soil-hot drought covariation and land-atmospheric pathway decomposition is linear and cannot capture nonlinear interactions. The neighbour sets are defined by continental proximity which may blur relevant remote source and sink of moisture and heat. Even so, this study establishes regional soil-moisture feedback, its spatial organisation, and its large-scale connectivity as first-order, evolving controls on hot-drought severity. This reframes intensifying hot drought risk as a multi-scale, non-stationary problem marking the Colorado–Rio Grande corridor as its most urgent natural laboratory.

Methods

Data and preprocessing. All fields are aligned on a common tensor $\mathbf{X} \in \mathbb{R}^{N_g \times N_y \times N_d}$ indexed by grid cell i, year j and warm-season day d, with $N_g = 44{,}531$ land cells at 0.5° resolution, $N_y = 44$ years (1980–2023) and $N_d = 183$ days (1 Apr–30 Sep). Sources are summarised in Table 1. Grids across CPC and ERA-5 are co-registered by exact coordinate matching and cells with $> 1\%$ missing values are dropped. Leap days are removed. Gaps of ≤ 5 days are linearly interpolated; longer gaps are filled with the climatological mean of a circular ±15-day, all-years window centred on the target day-of-year (DOY).

Table 1: Source datasets. Derived fields: $E = LE/L_v$ with Latent heat of vaporization: $L_v = 2.45 \times 10^6$ J kg^{-1}, LE is the latent heat E is the evaporation.

Field	**Source**	**Resolution**
Precipitation (P)	Climatic Prediction Center (CPC)	0.5°, daily
daily maximum temperature	CPC	0.5°, daily
Soil moisture (SM)	GLEAM v4.1a	0.1°, daily
latent heat	ERA5	0.1°, daily
500-mb geopotential height	ERA5	0.1°, daily
GMTA	GISTEMP/LOTI	annual

Calendar-day percentile thresholds $T^{(q)}_{i,\rho}$ ($q \in \{25, 75, 80, 90\}$) are computed on a centred ±2-day, 45-year pool (225 samples). The 75th percentile defines the heat threshold and $T^{(75)} - T^{(25)}$ provides an IQR scale for severity. Every continuous field X is additively decomposed into a DOY climatology $\bar{X}_{i,\rho}$, an 11-year centred running-mean trend $\tau_{i,t}$ of the deseasonalised series, and an anomaly $X'_{i,t} = X_{i,t} - \bar{X}_{i,\rho(t)} - \tau_{i,t}$; anomalies (SM$'$, Z'_{500}, E', T', P') enter all downstream regressions.

Compound dry–hot event definition. Daily hazard flags are $h_{i,j,d} = \mathbb{1}\{T_{\max} > T^{(75)}\}$ and $g_{i,j,d} = \mathbb{1}\{\mathrm{SPI} < -0.5\}$, with SPI a 12-week gamma-fitted standardised precipitation index. Their conjunction $c = h \wedge g$ becomes a persistent hot-drought event $e_{i,j,d}$ when it lasts ≥ 3 consecutive days. Per-day severity combines the IQR-normalised heat magnitude $m = (T_{\max} - T^{(25)})/(T^{(75)} - T^{(25)})$ with SPI depth,

$$s_{i,j,d} = -\, m_{i,j,d} \cdot \mathrm{SPI}_{i,j,d} \cdot e_{i,j,d}, \tag{1}$$

and the season-integrated severity $S_{i,j} = \sum_d s_{i,j,d}$ is the response variable in all subsequent regressions.

Soil-Hot Drought covariation Framework. For each cell–year, hot-drought severity is regressed on soil-moisture and Z_{500} anomalies over the N_d warm-season days,

$$s_{i,j,d} = \alpha_{i,j} + \delta_{1,i,j}\, \mathrm{SM}'_{i,j,d} + \delta_{2,i,j}\, Z'_{500,i,j,d} + \varepsilon_{i,j,d}, \tag{2}$$

with a per-year intercept. $\delta_1 < 0$ indicates soil-drying amplification of hot droughts; $\delta_2 > 0$ indicates ridge Define the active set $\mathcal{A}_{i,j} = \{d : \hat{y}_{i,j,d} > 0\}$ from the noise-free prediction; conditioning on $\hat{y}$ rather than observed severity avoids endogenous selection. Season-cumulative

SM contributions, carrying native hot-drought units, are

$$C_{\mathrm{SM}}(i,j) = \sum_{d\in\mathcal{A}_{i,j}} \delta_{1,i,j}\,\mathrm{SM}'_{i,j,d}, \qquad f_{\mathrm{SM}} = C_{\mathrm{SM}}/C_{\hat{y}}, \;\; C_{\hat{y}} = \sum_{d\in\mathcal{A}} \hat{y}_d, \tag{3}$$

and provide the seasonal-scale attribution used throughout.

Conditioned mediated feedback sensitivity (CMFS). Soil desiccation propagates into both heat and drought through evaporation: dry soil raises the Bowen ratio and reduces recycled moisture. A three-stage path model, each fitted by OLS formalises this mechanism with E' as the shared mediator,

$$E'_d = \mu^E + \alpha_1\,\mathrm{SM}'_d + \alpha_2 Z'_{500,d} + \varepsilon_d, \tag{4}$$
$$T'_d = \mu^T + \gamma_1 E'_d + \gamma_2\,\mathrm{SM}'_d + \gamma_3 Z'_{500,d} + \varepsilon_d, \tag{5}$$
$$P'_d = \mu^P + \phi_1 E'_d + \phi_2\,\mathrm{SM}'_d + \phi_3 Z'_{500,d} + \varepsilon_d. \tag{6}$$

The mediated composites $\mathrm{CMFS}_T = \alpha_1\gamma_1$ and $\mathrm{CMFS}_P = \alpha_1\phi_1$ and their season-cumulative contributions on the same active set $\mathcal{A}$,

$$C^T_{\mathrm{SM}}(i,j) = \sum_{d\in\mathcal{A}} \alpha_1\gamma_1\,\mathrm{SM}'_d, \qquad C^P_{\mathrm{SM}}(i,j) = \sum_{d\in\mathcal{A}} \alpha_1\phi_1\,\mathrm{SM}'_d, \tag{7}$$

carry temperature and precipitation units respectively. In the classical drought regime $\alpha_1 > 0$, $\gamma_1 < 0$, $\phi_1 > 0$, giving $\mathrm{CMFS}_T < 0$ (drying warms) and $\mathrm{CMFS}_P > 0$ (drying suppresses rain): a single soil perturbation transmitted into both hazards through evaporation.

Desiccation taxonomy. Each cell–year is classified into one of twelve mutually exclusive regimes using (i) the sign of the mediated composites—classical if $\mathrm{CMFS}_T < 0 \wedge \mathrm{CMFS}_P > 0$, non-classical if $\mathrm{CMFS}_T > 0 \wedge \mathrm{CMFS}_P < 0$; (ii) the realised direction from eq. 7, with $C^T_{\mathrm{SM}} > 0$ (*warmed*) and $C^P_{\mathrm{SM}} < 0$ (*dried*), compound desiccation requiring both; and (iii) sigma-normalised dominance $r_T = |C^T_{\mathrm{SM}}|/\sigma_T$, $r_P = |C^P_{\mathrm{SM}}|/\sigma_P$ with segment-level σ_T, σ_P, a cell–year being *balanced* when $\min(r_T, r_P) \geq 0.5\max(r_T, r_P)$. Full rule set in Table 2.

Table 2: Twelve-category desiccation taxonomy. "Both" inherits $\mathrm{CMFS}_T{<}0 \wedge \mathrm{CMFS}_P{>}0$; "non-cl" inherits $\mathrm{CMFS}_T{>}0 \wedge \mathrm{CMFS}_P{<}0$; "desicc" is warmed∧dried.

Class	**Rule**	**Physical meaning**
T1 Active thermal	$\mathrm{CMFS}_T{<}0$, $\mathrm{CMFS}_P{\leq}0$, $C^T_{\mathrm{SM}}{>}0$	Drying $\rightarrow E\downarrow\rightarrow$ warming
T2 Structural thermal	$\mathrm{CMFS}_T{<}0$, $\mathrm{CMFS}_P{\leq}0$, $C^T_{\mathrm{SM}}{\leq}0$	Wetting-based thermal suppression
P1 Active hydro	$\mathrm{CMFS}_T{\geq}0$, $\mathrm{CMFS}_P{>}0$, $C^P_{\mathrm{SM}}{<}0$	Drying $\rightarrow E\downarrow\rightarrow$ rain suppression
P2 Structural hydro	$\mathrm{CMFS}_T{\geq}0$, $\mathrm{CMFS}_P{>}0$, $C^P_{\mathrm{SM}}{\geq}0$	Wetting enhances precipitation
C TP Classical balanced	both, desicc, balanced	Both pathways soil-confirmed
C T Classical T-dom	both, desicc, ¬bal., $r_T{\geq}r_P$	Compound; thermal dominant
C P Classical P-dom	both, desicc, ¬bal., $r_T{<}r_P$	Compound; hydrological dominant
C X Classical wetting	both, ¬desicc	Classical wiring, wetting realised
N TP Non-cl. balanced	non-cl, warmed, balanced	Inverted wiring; balanced
N T Non-cl. T-dom	non-cl, warmed, ¬bal., $r_T{\geq}r_P$	Inverted; thermal dominant
N P Non-cl. P-dom	non-cl, warmed, ¬bal., $r_T{<}r_P$	Inverted; hydrological dominant
N X Non-cl. neutral	non-cl, ¬warmed	Inverted; no warming realised

Basin Regression Thirty major rivers are partitioned into Upper/Middle/Lower segments (81 segments; nine rivers have only two) using HydroRIVERS polygons; grid-cell membership requires the centroid to lie inside the segment's convex hull, with a minimum of five cells. Segment-mean fields $\bar{X}_{s,j,d} = |I_s|^{-1} \sum_{i\in I_s} X_{i,j,d}$ enter the identical fitting kernel used at the grid scale, so basin coefficients are numerically consistent with spatial composites of grid fits. The taxonomy of Table 2 is applied per segment–year to yield basin-scale regime trajectories.

Spatial-clustering moderation. Two segments with equal mean SM deficit can differ in coherence: only a spatially contiguous deficit sustains the sensible-heat flux and moisture suppression required for a persistent heat dome. For each segment a row-normalised adjacency $\mathbf{W}$ is built from a k-d-tree on member grid cells (edges within 1.5 times the median first-nearest-neighbour distance), and the daily Moran's I of driver X is

$$I_X(d) = \frac{|I_s|}{S_0} \cdot \frac{\sum_{a,b} W_{ab}\, z_a(d)\, z_b(d)}{\sum_a z_a(d)^2}, \quad z_a(d) = X_a(d) - \bar{X}(d), \;\; S_0 = \sum_{a,b} W_{ab}. \tag{8}$$

The amplitude-modulated coherence index $M_X(d) = -I_X(d) \cdot X'(d)$ combines coherence and amplitude; for SM under drought ($\mathrm{SM}' < 0$), $M_{\mathrm{SM}}(d) > 0$ identifies days that are both coherently and anomalously dry. Restricted to $\mathcal{A}$, the residual of eq. 2 is regressed on the moderator pair,

$$\hat{\varepsilon}_{\mathrm{simple}}(d) = \beta_I\, I_{\mathrm{SM}}(d) + \beta_M\, M_{\mathrm{SM}}(d) + \eta(d), \quad d \in \mathcal{A}, \tag{9}$$

yielding the active-day $R^2_{\mathrm{aug,act}}$ and the incremental $\Delta R^2_{\mathrm{aug,act}}$ contributed by the amplitude-interaction term.

Cross-basin propagation. A neighbour set $\mathcal{N}(i)$ is defined as the union of (a) other segments of the same river and (b) all segments in the same physico-climatic cluster of Table 3. Neighbour-mean anomaly fields $\bar{\Phi}_{E',i}(d) = |\mathcal{N}(i)|^{-1} \sum_{j\in\mathcal{N}(i)} E'_j(d)$ and $\bar{\Psi}_{T',i}(d) = |\mathcal{N}(i)|^{-1} \sum_{j\in\mathcal{N}(i)} T'_j(d)$ serve as imported-moisture and advected-warming proxies. To guarantee that propagation explains variance not already claimed locally, the OLS residual is first purged of the within-basin clustering signal by a no-intercept fit on z-scored Moran's I_k and mean-centred interaction products for $k \in \{\mathrm{SM}, Z_{500}\}$; its residual ε^1 is the post-local residual. Restricted to $\mathcal{A}$, the propagation regression is

$$\varepsilon^1_i(d) = \lambda_E\, \bar{\Phi}_{E',i}(d) + \mu_T\, \bar{\Psi}_{T',i}(d) + \eta(d), \quad d \in \mathcal{A}_i, \tag{10}$$

fitted without intercept with HAC standard errors ($L = 5$). The propagation hypothesis predicts $\lambda_E < 0$ (neighbour evaporation deficits raise the local residual) and $\mu_T > 0$ (advective warming from connected basins raises it).

Hierarchical variance cascade. The three estimators partition hot-drought variance orthogonally by construction, each fitted on the residual of the previous tier: Tier 1—local OLS (eq. 2), $R^2_s \equiv R^2_{\mathrm{simple}}$; Tier 2—amplitude-modulated within-basin clustering (eq. 9), $\Delta R^2_{\mathrm{aug,act}}$; Tier 3—cross-basin propagation (eq. 10), $\Delta R^2_{\mathrm{prop}}$. Because each increment acts on a successively

Table 3: Between-basin physico-climatic clusters defining $\mathcal{N}(i)$.

Cluster	**Member rivers**
South Asian Monsoon	Indus, Ganges, Brahmaputra, Yangtze, Yellow, Mekong, Irrawaddy
East Asian Monsoon	Yangtze, Yellow, Mekong, Amur
Tropical S. America	Amazon, Orinoco, Tocantins, São Francisco
La Plata	Paraná, Amazon
SW North America	Colorado, Rio Grande
Tropical Africa	Congo, Niger, Nile, Zambezi
Southern Africa	Zambezi, Orange
European Temperate	Danube, Rhine, Dnieper, Volga
Middle East Arid	Tigris–Euphrates, Indus
Pacific Northwest	Columbia, St. Lawrence
Australian Dryland	Murray–Darling, Fly

smaller residual, the double-count-free total is

$$R^2_{\text{total}} = R^2_s + \Delta R^2_{\text{aug,act}}\,(1 - R^2_s) + \Delta R^2_{\text{prop}}\,(1 - R^2_s)(1 - \Delta R^2_{\text{aug,act}}). \tag{11}$$

Trend analysis. For every annual scalar time series—δ_1, $\text{CMFS}_{T,P}$, $C^{T,P}_{\text{SM}}$, $R^2_{\text{aug,act}}$, $\bar{M}_{\text{SM}}$, λ_E, μ_T, and each tier of eq. 11—a Theil–Sen slope and a Mann–Kendall p are reported over 1980–2023. Bivariate trend spaces partition segments into four physically labelled quadrants: for the propagation trend, $(\partial_t\lambda_E, \partial_t\mu_T) \in \{(-,+),(-,-),(+,+),(+,-)\}$ correspond to canonical strengthening, moisture-dominated, warming-dominated and decoupling regimes, respectively; for the clustering trend, $(\partial_t R^2_{\text{aug,act}}, \partial_t\bar{M}_{\text{SM}})$ analogously labels amplification, efficiency, decoupled-growth and decoupling regimes. All maps use Robinson projection with the HydroRIVERS polygon layer.

Fixed parameters. HAC Bartlett lag $L = 5$; trend running-mean window $W = 11$ yr; block-bootstrap length $b = 14$ d with $B = 1{,}000$ replicates; active-day threshold $\tau = 0$; SPI window 12 wk; heat threshold at the 75th DOY percentile.

References

[1] Toby R Ault. On the essentials of drought in a changing climate. *Science*, 368(6488):256–260, 2020.

[2] Somnath Mondal, Ashok K. Mishra, Ruby Leung, and Benjamin Cook. Global droughts connected by linkages between drought hubs. *Nature Communications*, 14(1):144, 2023.

[3] Ashok K Mishra and Vijay P Singh. A review of drought concepts. *Journal of hydrology*, 391(1-2):202–216, 2010.

[4] Solomon H Gebrechorkos, Justin Sheffield, Sergio M Vicente-Serrano, Chris Funk, Diego G Miralles, Jian Peng, Ellen Dyer, Joshua Talib, Hylke E Beck, Michael B Singer, et al. Warming accelerates global drought severity. *Nature*, 642(8068):628–635, 2025.

[5] Cristian Martinez-Villalobos, Danning Fu, Paul C Loikith, and J David Neelin. Accel-

erating increase in the duration of heatwaves under global warming. *Nature Geoscience*, 18(8):716–723, 2025.

[6] John Nairn and Simon J Mason. Extreme heat and heatwaves: hazard awareness and impact mitigation. *The Lancet Planetary Health*, 9(7), 2025.

[7] Daniela IV Domeisen, Elfatih AB Eltahir, Erich M Fischer, Reto Knutti, Sarah E Perkins-Kirkpatrick, Christoph Schär, Sonia I Seneviratne, Antje Weisheimer, and Heini Wernli. Prediction and projection of heatwaves. *Nature Reviews Earth & Environment*, 4(1):36–50, 2023.

[8] Somnath Mondal and Enrique R Vivoni. Hot drought of summer 2023 in southwestern north america. *Geophysical Research Letters*, 52(18):e2025GL118308, 2025.

[9] Sourav Mukherjee and Ashok Kumar Mishra. Increase in compound drought and heatwaves in a warming world. *Geophysical Research Letters*, 48(1):e2020GL090617, 2021.

[10] Mahnaz Afroz, Gang Chen, and Aavudai Anandhi. Drought-and heatwave-associated compound extremes: A review of hotspots, variables, parameters, drivers, impacts, and analysis frameworks. *Frontiers in Earth Science*, 10:914437, 2023.

[11] Xingwang Fan, Yunlin Zhang, Kun Shi, Jian Peng, Yongwei Liu, Yongqiang Zhou, Yuanbo Liu, Qing Zhu, Chunqiao Song, Rongrong Wan, et al. Surging compound drought–heatwaves underrated in global soils. *Proceedings of the National Academy of Sciences*, 121(42):e2410294121, 2024.

[12] Jiabo Yin, Pierre Gentine, Louise Slater, Lei Gu, Yadu Pokhrel, Naota Hanasaki, Shenglian Guo, Lihua Xiong, and Wolfram Schlenker. Future socio-ecosystem productivity threatened by compound drought–heatwave events. *Nature Sustainability*, 6(3):259–272, 2023.

[13] Jun Wang, Ran Yan, Guoxiong Wu, Yimin Liu, Meirong Wang, Ning Zeng, Fei Jiang, Hengmao Wang, Wei He, Mousong Wu, et al. Unprecedented decline in photosynthesis caused by summer 2022 record-breaking compound drought-heatwave over yangtze river basin. *Science Bulletin*, 68(19):2160–2163, 2023.

[14] Corey Lesk, Weston Anderson, Angela Rigden, Onoriode Coast, Jonas Jägermeyr, Sonali McDermid, Kyle F Davis, and Megan Konar. Compound heat and moisture extreme impacts on global crop yields under climate change. *Nature Reviews Earth & Environment*, 3(12):872–889, 2022.

[15] Anqian Wang, Hui Tao, Gang Ding, Baolei Zhang, Jinlong Huang, and Quanyuan Wu. Global cropland exposure to extreme compound drought heatwave events under future climate change. *Weather and Climate Extremes*, 40:100559, 2023.

[16] Duncan J Graham, Marc FP Bierkens, and Michelle TH van Vliet. Impacts of droughts and heatwaves on river water quality worldwide. *Journal of Hydrology*, 629:130590, 2024.

[17] Gabriel A Cárdenas Belleza, Marc FP Bierkens, and Michelle TH Van Vliet. Sectoral

water use responses to droughts and heatwaves: analyses from local to global scales for 1990–2019. *Environmental Research Letters*, 18(10):104008, 2023.

[18] Samuel Jonson Sutanto, Claudia Vitolo, Claudia Di Napoli, Mirko D'Andrea, and Henny AJ Van Lanen. Heatwaves, droughts, and fires: Exploring compound and cascading dry hazards at the pan-european scale. *Environment international*, 134:105276, 2020.

[19] Boen Zhang, Shuo Wang, and Louise Slater. Anthropogenic climate change doubled the frequency of compound drought and heatwaves in low-income regions. *Communications Earth & Environment*, 5(1):715, 2024.

[20] João L Geirinhas, Ana Russo, Renata Libonati, Pedro M Sousa, Diego G Miralles, and Ricardo M Trigo. Recent increasing frequency of compound summer drought and heatwaves in southeast brazil. *Environmental Research Letters*, 16(3):034036, 2021.

[21] Yi Yang and Jianping Tang. Process-oriented compound long-duration dry and hot events in china: Atmospheric conditions, moisture, and heat budget analyses. *Journal of Climate*, 37(19):5131–5151, 2024.

[22] Monica Ionita, Diana E Caldarescu, and Viorica Nagavciuc. Compound hot and dry events in europe: variability and large-scale drivers. *Frontiers in Climate*, 3:688991, 2021.

[23] Paul A Dirmeyer, Gianpaolo Balsamo, Eleanor M Blyth, Ross Morrison, and Hollie M Cooper. Land-atmosphere interactions exacerbated the drought and heatwave over northern europe during summer 2018. *Agu Advances*, 2(2):e2020AV000283, 2021.

[24] Kexin Gui, Tianjun Zhou, Wenxia Zhang, and Xing Zhang. Land-atmosphere coupling amplified the record-breaking heatwave at altitudes above 5000 meters on the tibetan plateau in july 2022. *Weather and Climate Extremes*, 45:100717, 2024.

[25] Yueyang Ni, Bo Qiu, Xin Miao, Lingfeng Li, Jiuyi Chen, Xiaohui Tian, Siwen Zhao, and Weidong Guo. Shift of soil moisture-temperature coupling exacerbated 2022 compound hot-dry event in eastern china. *Environmental Research Letters*, 19(1):014059, 2024.

[26] Mehdi Rahmati, Wulf Amelung, Cosimo Brogi, Jacopo Dari, Alessia Flammini, Heye Bogena, Luca Brocca, Hao Chen, Jannis Groh, Randal D Koster, et al. Soil moisture memory: State-of-the-art and the way forward. *Reviews of Geophysics*, 62(2):e2023RG000828, 2024.

[27] Donghyuck Yoon, Jan-Huey Chen, Hsin Hsu, and Kirsten L Findell. Variations in land-atmosphere coupling during drought-heatwave events. *Communications Earth & Environment*, 7(1):1, 2026.

[28] Karen E King, Edward R Cook, Kevin J Anchukaitis, Benjamin I Cook, Jason E Smerdon, Richard Seager, Grant L Harley, and Benjamin Spei. Increasing prevalence of hot drought across western north america since the 16th century. *Science Advances*, 10(4):eadj4289, 2024.

[29] Amal Joy and K Satheesan. Influence of soil moisture on mean daily maximum and minimum temperatures over india. *Meteorology and Atmospheric Physics*, 134(3):49, 2022.

[30] Xing Chen and Su-Jong Jeong. Irrigation enhances local warming with greater nocturnal warming effects than daytime cooling effects. *Environmental research letters*, 13(2):024005, 2018.

[31] Vimal Mishra, Anukesh Krishnankutty Ambika, Akarsh Asoka, Saran Aadhar, Jonathan Buzan, Rohini Kumar, and Matthew Huber. Moist heat stress extremes in india enhanced by irrigation. *Nature Geoscience*, 13(11):722–728, 2020.

[32] Qinqin Kong and Matthew Huber. Regimes of soil moisture–wet-bulb temperature coupling with relevance to moist heat stress. *Journal of Climate*, 36(22):7925–7942, 2023.

[33] Guillaume Chagnaud, Christopher M Taylor, Lawrence Stephen Jackson, CE Birch, JH Marsham, and Cornelia Klein. Wet-bulb temperature extremes locally amplified by wet soils. *Geophysical Research Letters*, 52(8):e2024GL112467, 2025.

[34] Weicheng Liu, Qiang Zhang, Chenrui Li, Lili Xu, and Wei Xiao. The influence of soil moisture on convective activity: a review. *Theoretical and Applied Climatology*, 149(1):221–232, 2022.

[35] Tat Fan Cheng and Mengqian Lu. Global lagrangian tracking of continental precipitation recycling, footprints, and cascades. *Journal of Climate*, 36(6):1923–1941, 2023.

[36] Rudi J Van der Ent, Hubert HG Savenije, Bettina Schaefli, and Susan C Steele-Dunne. Origin and fate of atmospheric moisture over continents. *Water Resources Research*, 46(9), 2010.

[37] James S Famiglietti, Dongryeol Ryu, Aaron A Berg, Matthew Rodell, and Thomas J Jackson. Field observations of soil moisture variability across scales. *Water Resources Research*, 44(1), 2008.

[38] Ulrike Rosenbaum, Heye R Bogena, Michael Herbst, Johan A Huisman, Timothy J Peterson, Ansgar Weuthen, Andrew W Western, and Harry Vereecken. Seasonal and event dynamics of spatial soil moisture patterns at the small catchment scale. *Water resources research*, 48(10), 2012.

[39] B Li and M Rodell. Spatial variability and its scale dependency of observed and modeled soil moisture over different climate regions. *Hydrology and Earth System Sciences*, 17(3):1177–1188, 2013.

[40] Somnath Mondal and Ashok Mishra. Quantifying the precipitation, evapotranspiration, and soil moisture network's interaction over global land surface hydrological cycle. *Water Resources Research*, 60(2):e2023WR034861, 2024.

[41] K Sakaguchi, LK Berg, J Chen, J Fast, R Newsom, S-L Tai, Z Yang, WI Gustafson Jr, BJ Gaudet, M Huang, et al. Determining spatial scales of soil moisture—cloud coupling

pathways using semi-idealized simulations. *Journal of Geophysical Research: Atmospheres*, 127(2):e2021JD035282, 2022.

[42] Dominik L Schumacher, Jessica Keune, Paul Dirmeyer, and Diego G Miralles. Drought self-propagation in drylands due to land–atmosphere feedbacks. *Nature Geoscience*, 15(4):262–268, 2022.

[43] Dominik L Schumacher, Jessica Keune, Chiel C Van Heerwaarden, Jordi Vilà-Guerau de Arellano, Adriaan J Teuling, and Diego G Miralles. Amplification of mega-heatwaves through heat torrents fuelled by upwind drought. *Nature Geoscience*, 12(9):712–717, 2019.

[44] Haiyan Teng, Grant Branstator, Ahmed B Tawfik, and Patrick Callaghan. Circumglobal response to prescribed soil moisture over north america. *Journal of Climate*, 32(14):4525–4545, 2019.

[45] Jeffrey Q Chambers, Adriano José Nogueira Lima, Gilberto Pastorello, Bruno Oliva Gimenez, Lin Meng, Lee A Dyer, Yanlei Feng, Cristina Santos da Silva, Regison Costa de Oliveira, Anna Weber, et al. Hot droughts in the amazon provide a window to a future hypertropical climate. *Nature*, 649(8099):1190–1196, 2026.

Supplementary Information for
Multiscale land-atmospheric feedbacks intensify hot droughts over global river-basins

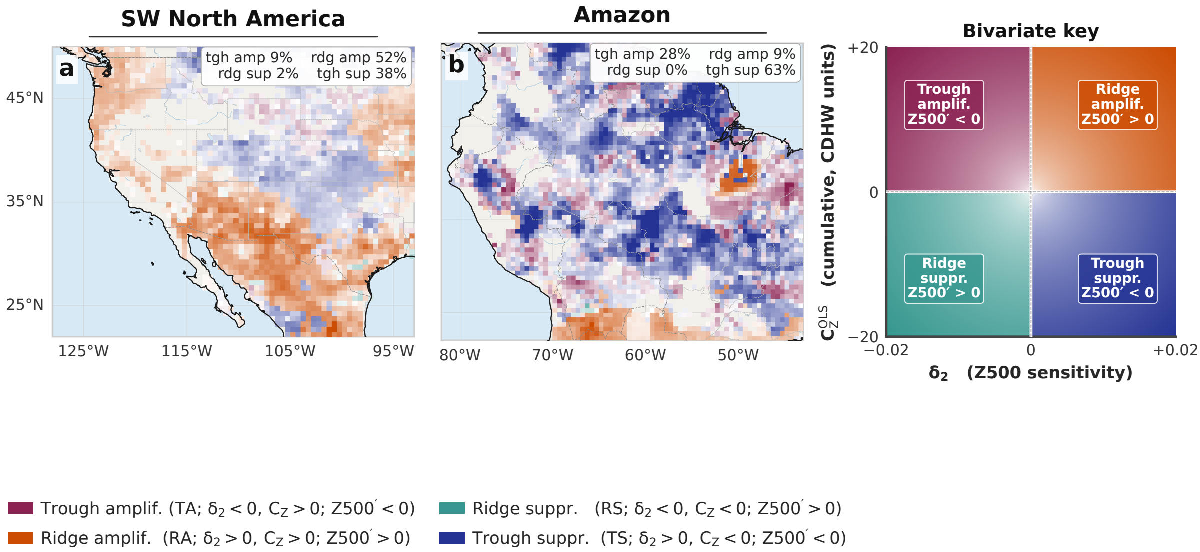

Supplementary Figure 1: Where and how strongly 500-mb geopotential height anomaly is associated with hot drought severity in south-western North America (a) and the Amazon (b).Each grid cell is coloured by two quantities simultaneously: δ_2 and $C_{\mathrm{Z}_{500}}$.

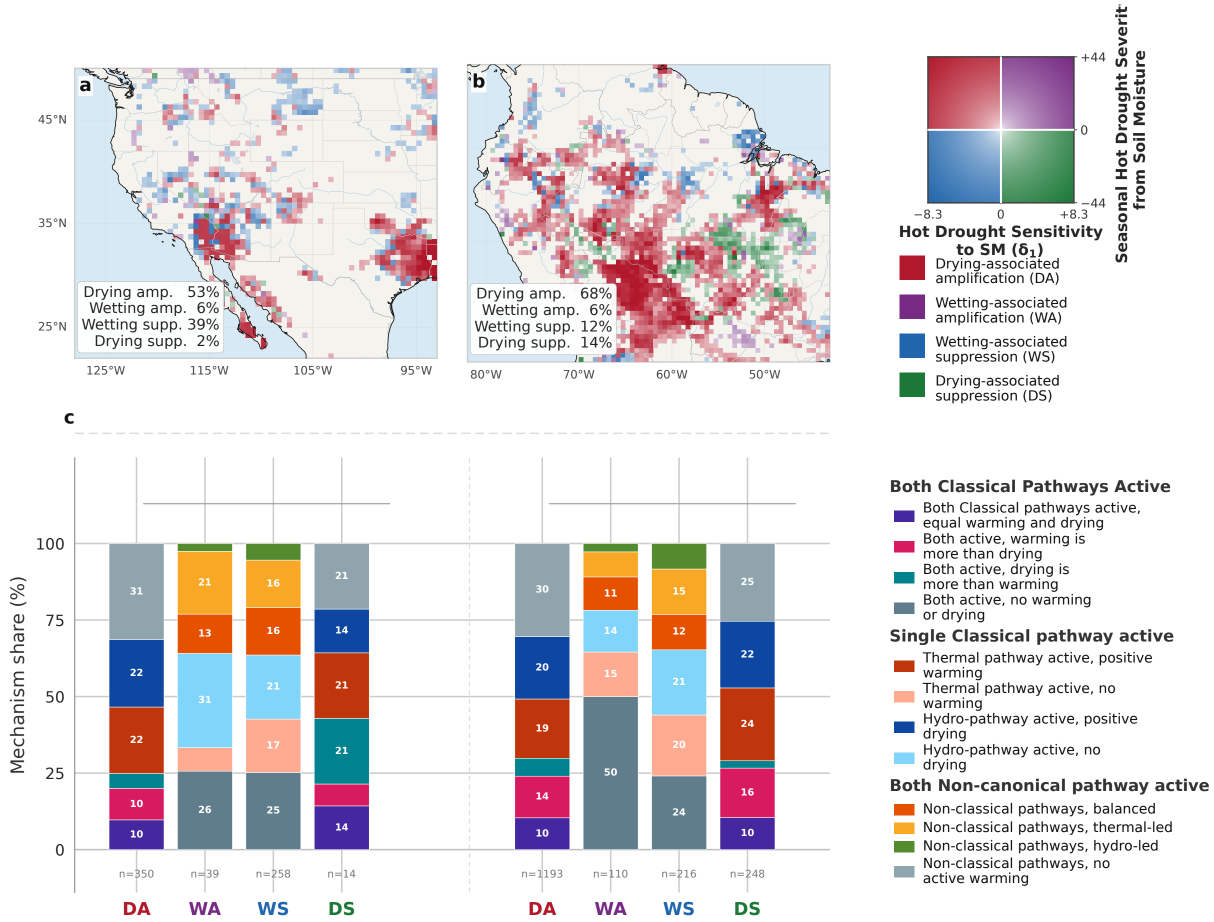

Supplementary Figure 2: Where and how strongly soil moisture is associated with hot drought severity in south-western North America (a) and the Amazon (b) in 2010 .Each grid cell is coloured by two quantities simultaneously: δ_1 and C_{SM}. Red (blue) tones indicate that dry (wet) soil is associated heat extremes. Color saturation reflects signal strength.(c,d) For each coupling regime identified in panels (a,b), the bars show what heterogenity in land-atmospheric feedback pathway of grid cells experienced.

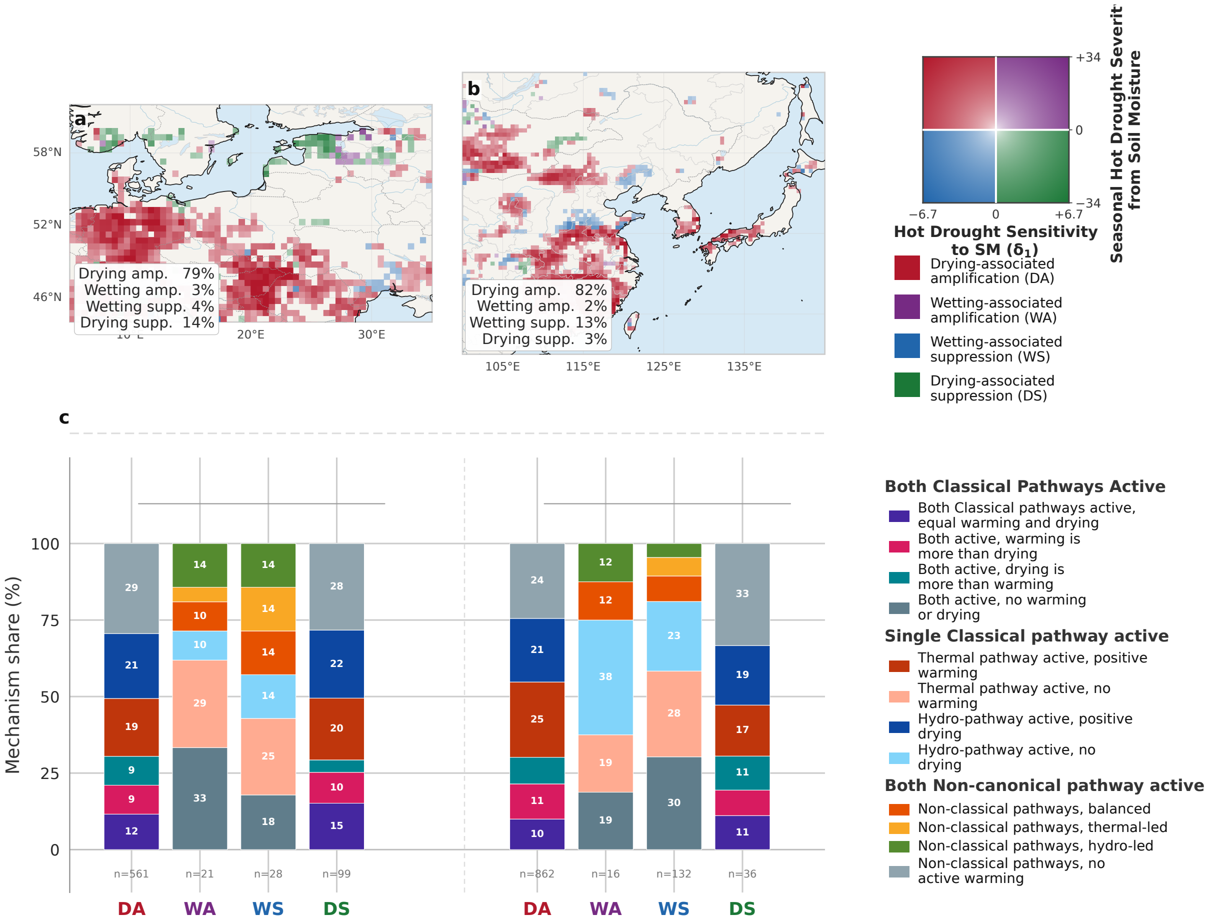

Supplementary Figure 3: Where and how strongly soil moisture is associated with hot drought severity in Central Europe (a) and (b) East in 2022 .Each grid cell is coloured by two quantities simultaneously: δ_1 and C_{SM}. Red (blue) tones indicate that dry (wet) soil is associated heat extremes. Color saturation reflects signal strength.(c,d) For each coupling regime identified in panels (a,b), the bars show what heterogenity in land-atmospheric feedback pathway of grid cells experienced.

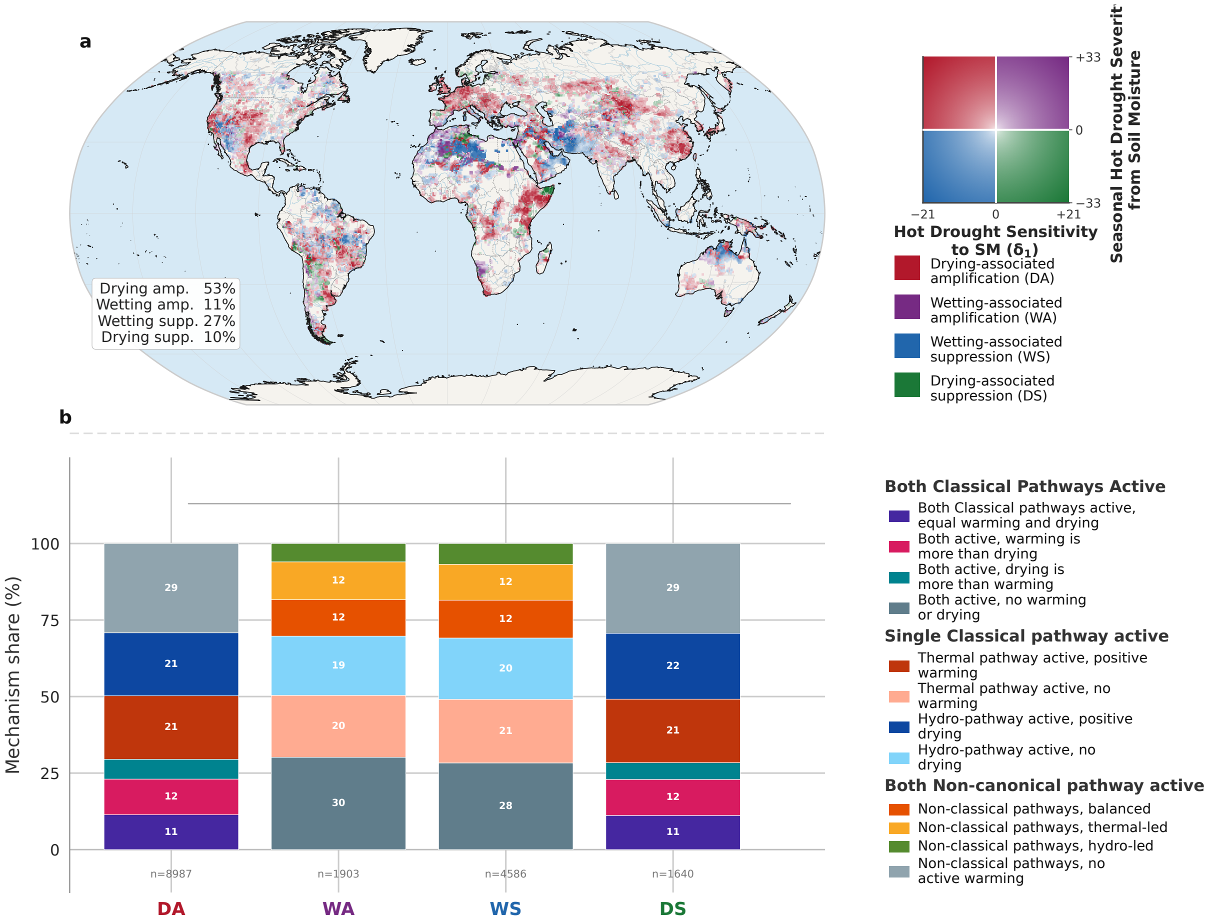

Supplementary Figure 4: Where and how strongly soil moisture is associated with hot drought severity in over the (a) globe in 2022 .Each grid cell is coloured by two quantities simultaneously: δ_1 and C_{SM}. Red (blue) tones indicate that dry (wet) soil is associated heat extremes. Color saturation reflects signal strength.(b) For each coupling regime identified in panels (a), the bars show what heterogenity in land-atmospheric feedback pathway of grid cells experienced.

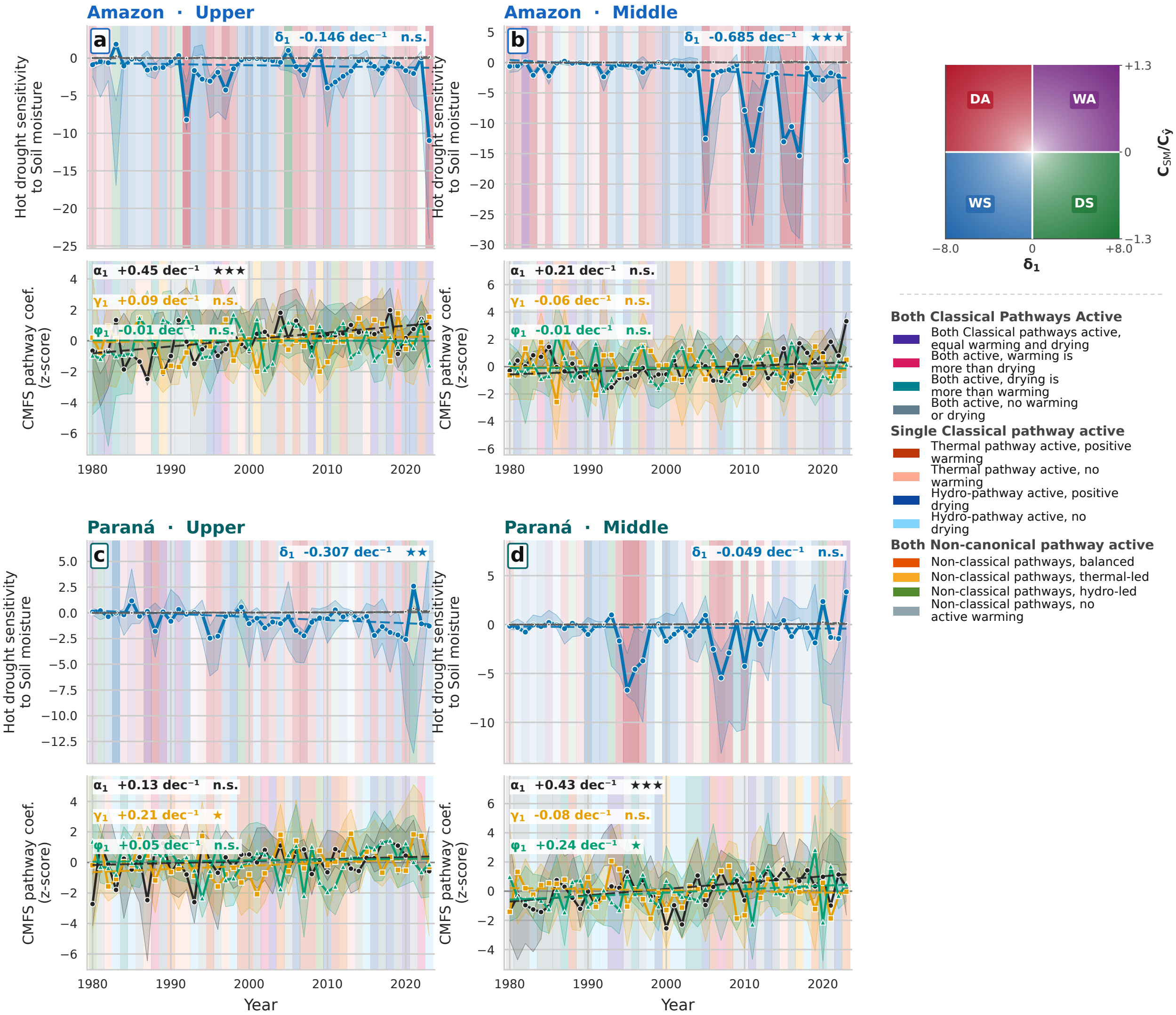

Supplementary Figure 5: (a–d) time series of soil-moisture-hot drought and land-atmospheric (CMFS) coupling coefficients for four river basin segments: Amazon Upper (a), Amazon Middle (b), Parana upper (c), Parana middle (d). Each panel pair shows two quantities.Upper sub-panel shows the sensitivity of hot drought severity to SM′ (δ_1, blue) with dashed lines showing Theil–Sen trends; background colour encodes the soil-hot drought coupling regime in each year. Lower sub-panel shows z-scored land–atmosphere pathway coefficients: sensitivity of evaporation to soil moisture (α_1), daily maximum temperature to evaporation (γ_1), and precipitation to evaporation (φ_1). Background shading indicates the LA feedback pathway in each year

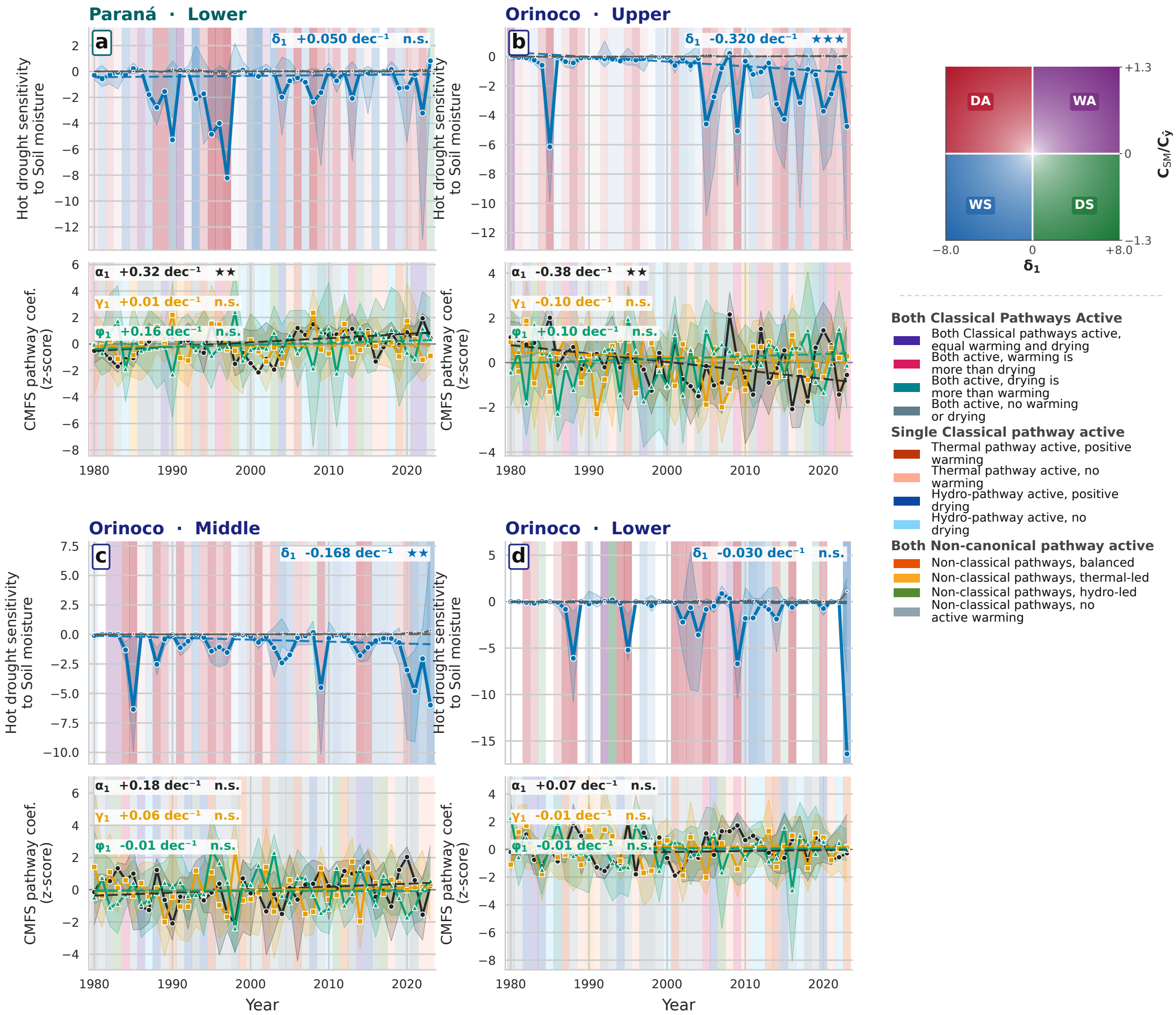

Supplementary Figure 6: (a–d) time series of soil-moisture-hot drought and land-atmospheric (CMFS) coupling coefficients for four river basin segments: Parana lower (a), Orinoco upper (b), Orinoco middle (c), Orinoco lower (d). Each panel pair shows two quantities.Upper sub-panel shows the sensitivity of hot drought severity to SM′ (δ_1, blue) with dashed lines showing Theil–Sen trends; background colour encodes the soil-hot drought coupling regime in each year. Lower sub-panel shows z-scored land–atmosphere pathway coefficients: sensitivity of evaporation to soil moisture (α_1), daily maximum temperature to evaporation (γ_1), and precipitation to evaporation (φ_1). Background shading indicates the LA feedback pathway in each year

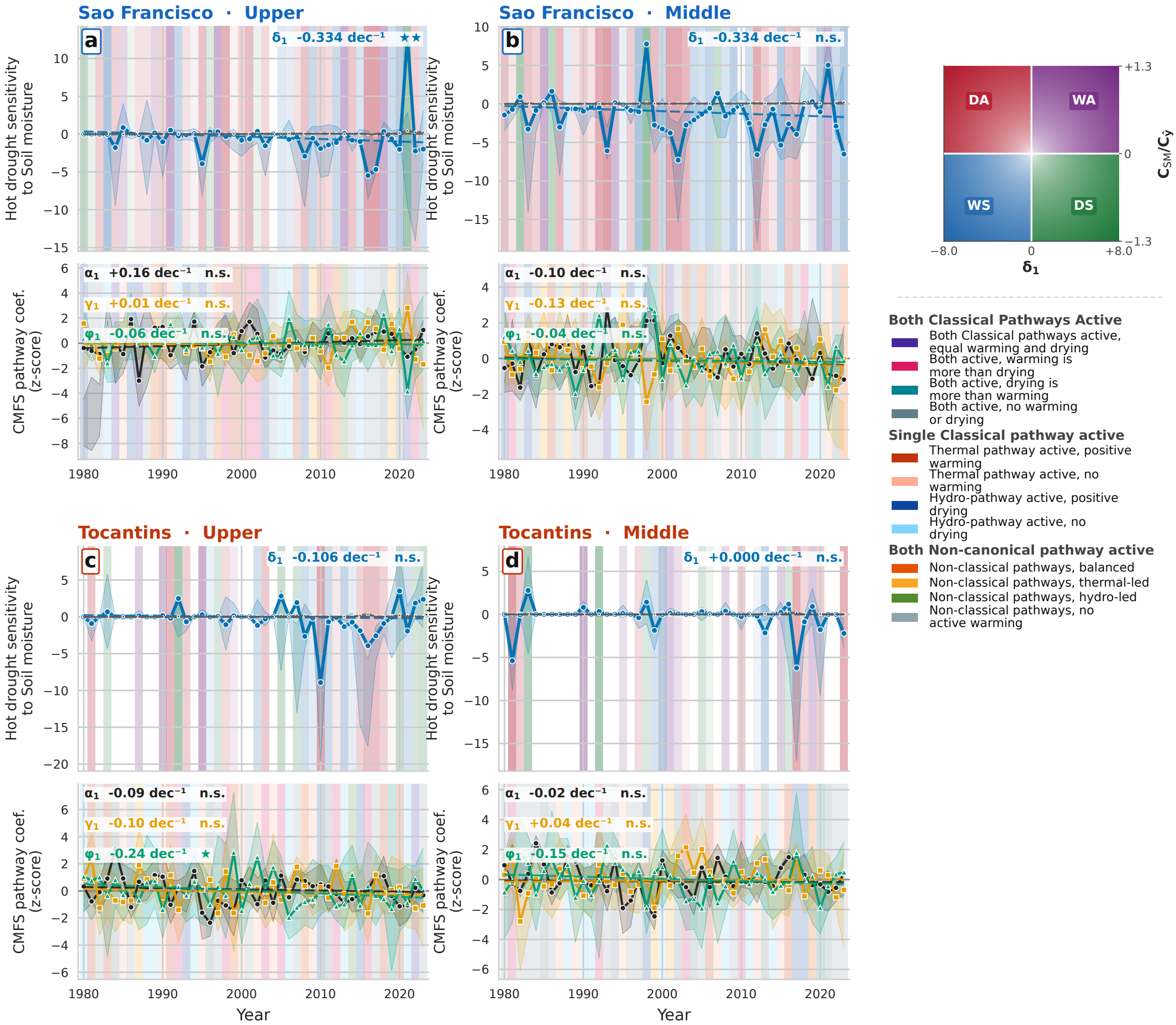

Supplementary Figure 7: (a–d) time series of soil-moisture-hot drought and land-atmospheric (CMFS) coupling coefficients for four river basin segments: Sao Francisco upper (a), Sao Francisco middle (b), Tocantins upper (c), Tocantins middle (d). Each panel pair shows two quantities.Upper sub-panel shows the sensitivity of hot drought severity to SM′ (δ_1, blue) with dashed lines showing Theil–Sen trends; background colour encodes the soil-hot drought coupling regime in each year. Lower sub-panel shows z-scored land–atmosphere pathway coefficients: sensitivity of evaporation to soil moisture (α_1), daily maximum temperature to evaporation (γ_1), and precipitation to evaporation (φ_1). Background shading indicates the LA feedback pathway in each year

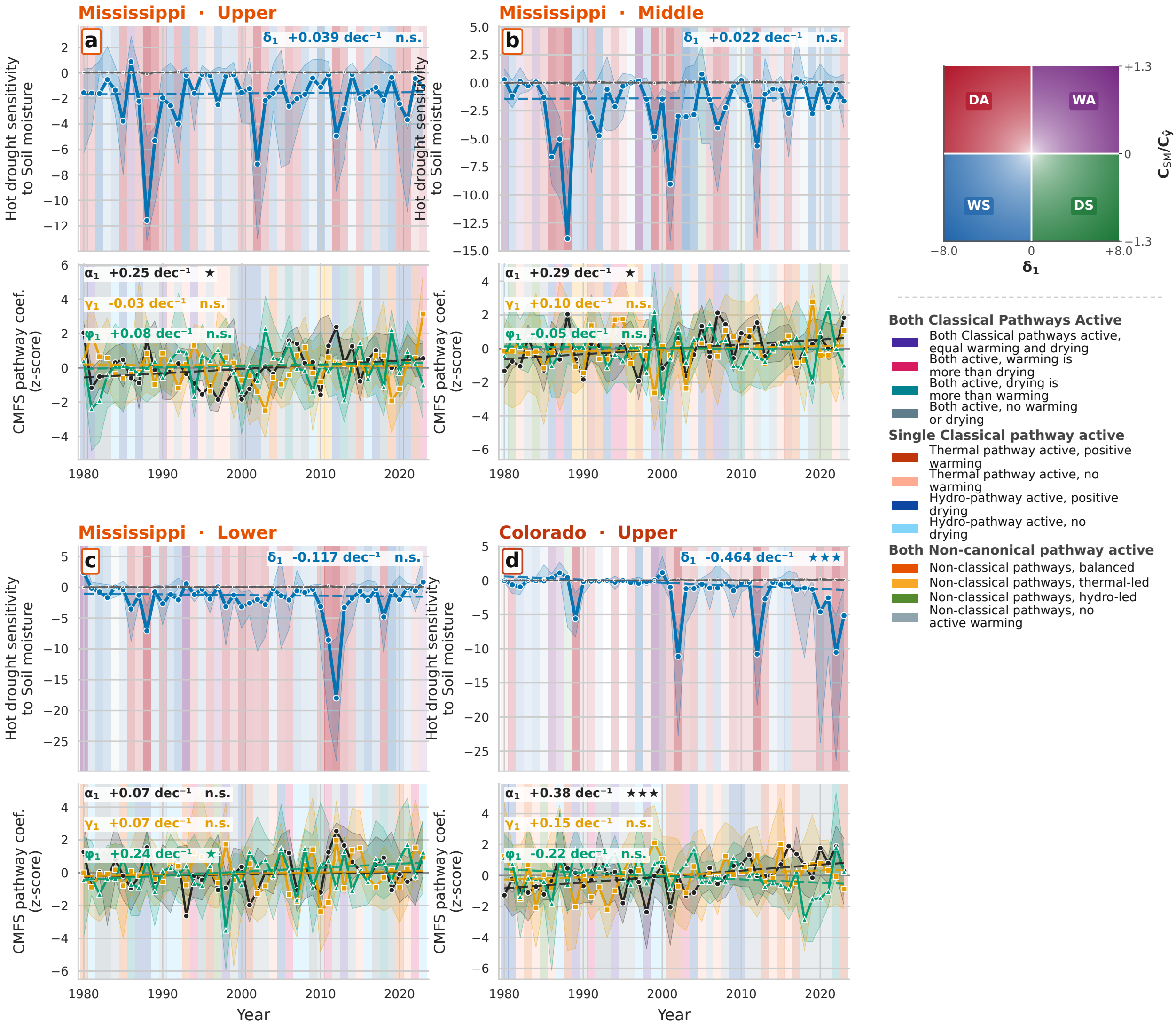

Supplementary Figure 8: (a–d) time series of soil-moisture-hot drought and land-atmospheric (CMFS) coupling coefficients for four river basin segments: Mississippi upper (a), Mississippi middle (b), Mississippi lower (c), Colorado upper (d). Each panel pair shows two quantities.Upper sub-panel shows the sensitivity of hot drought severity to SM′ (δ_1, blue) with dashed lines showing Theil–Sen trends; background colour encodes the soil-hot drought coupling regime in each year. Lower sub-panel shows z-scored land–atmosphere pathway coefficients: sensitivity of evaporation to soil moisture (α_1), daily maximum temperature to evaporation (γ_1), and precipitation to evaporation (φ_1). Background shading indicates the LA feedback pathway in each year

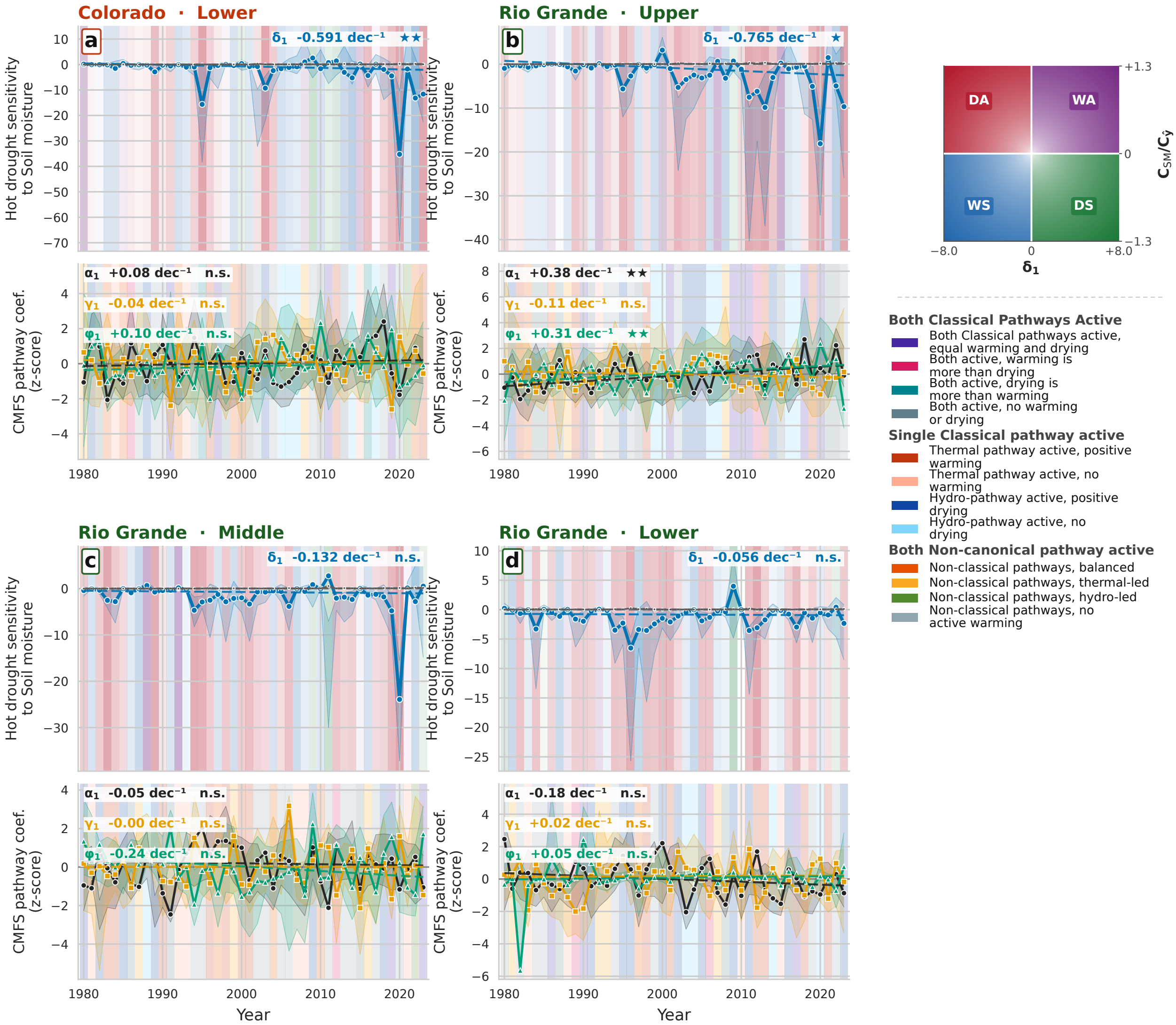

Supplementary Figure 9: (a–d) time series of soil-moisture-hot drought and land-atmospheric (CMFS) coupling coefficients for four river basin segments: Colorado lower (a), Rio grande Upper (b), Riograde middle (c), Riogrande lower(d). Each panel pair shows two quantities.Upper sub-panel shows the sensitivity of hot drought severity to SM′ (δ_1, blue) with dashed lines showing Theil–Sen trends; background colour encodes the soil-hot drought coupling regime in each year. Lower sub-panel shows z-scored land–atmosphere pathway coefficients: sensitivity of evaporation to soil moisture (α_1), daily maximum temperature to evaporation (γ_1), and precipitation to evaporation (φ_1). Background shading indicates the LA feedback pathway in each year

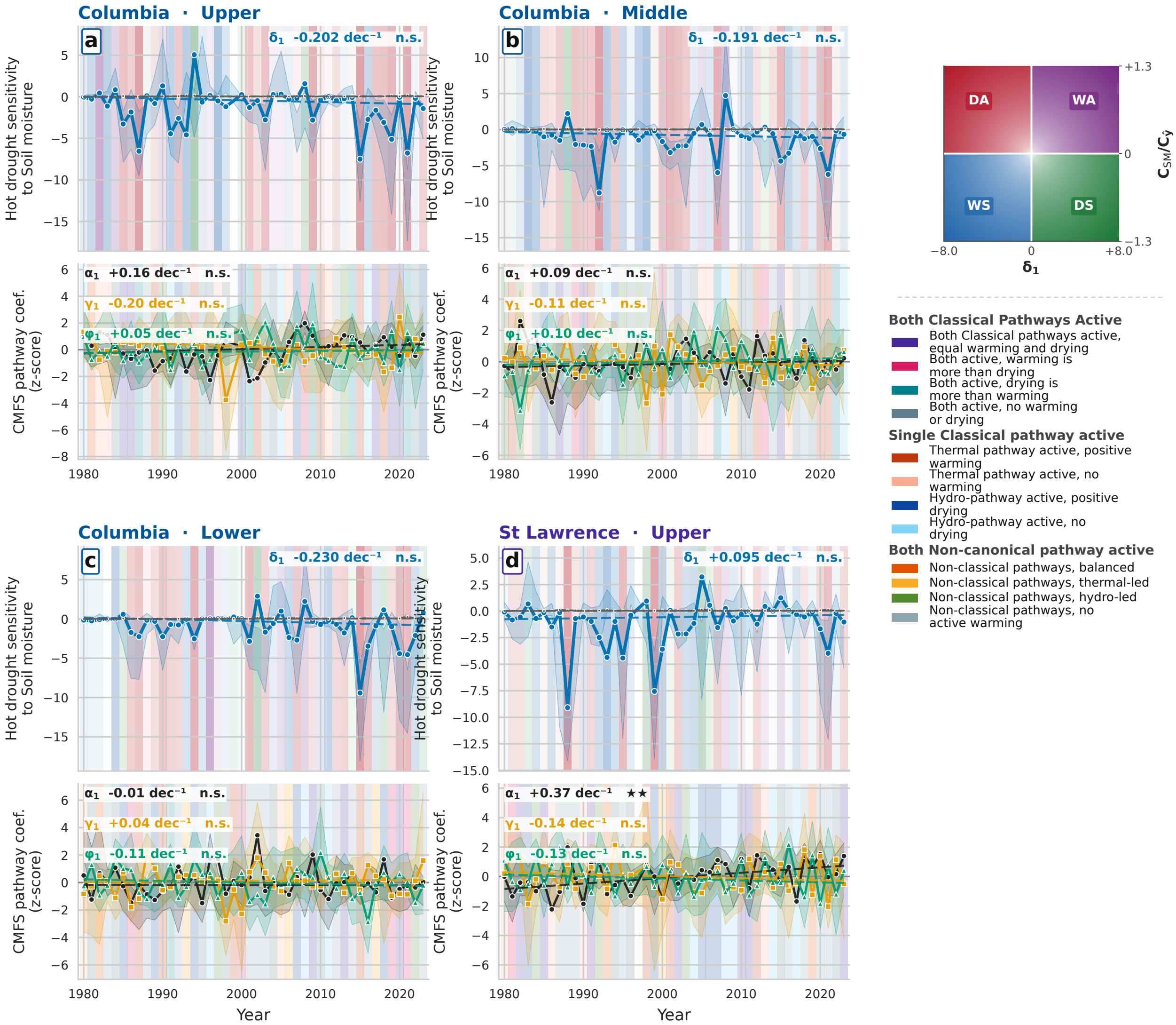

Supplementary Figure 10: (a–d) time series of soil-moisture-hot drought and land-atmospheric (CMFS) coupling coefficients for four river basin segments: Columbia Upper (a), Columbia middle (b), Columbia Upper (c), St. Lawrence Upper(d). Each panel pair shows two quantities.Upper sub-panel shows the sensitivity of hot drought severity to SM′ (δ_1, blue) with dashed lines showing Theil–Sen trends; background colour encodes the soil-hot drought coupling regime in each year. Lower sub-panel shows z-scored land–atmosphere pathway coefficients: sensitivity of evaporation to soil moisture (α_1), daily maximum temperature to evaporation (γ_1), and precipitation to evaporation (φ_1). Background shading indicates the LA feedback pathway in each year

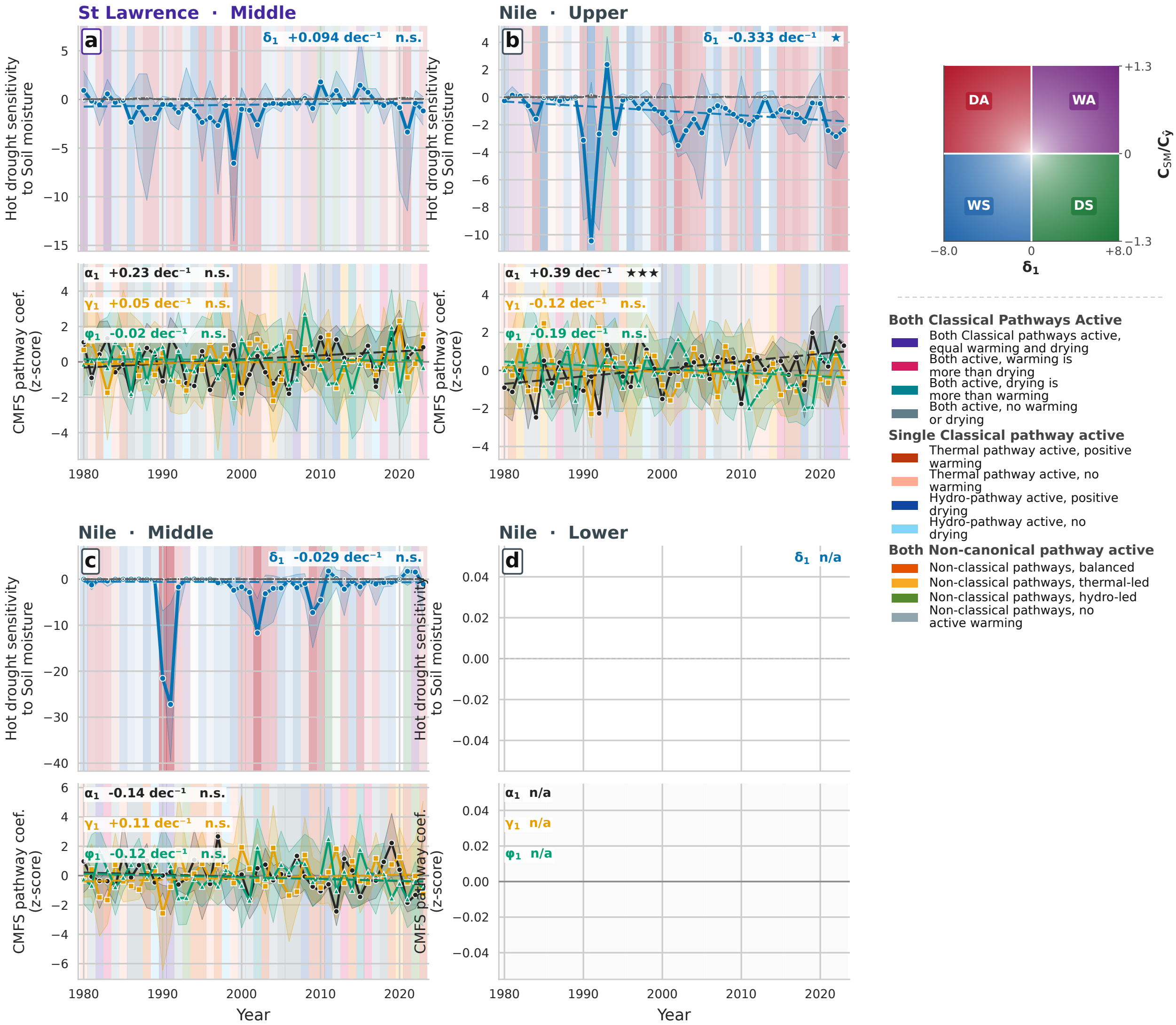

Supplementary Figure 11: (a–d) time series of soil-moisture-hot drought and land-atmospheric (CMFS) coupling coefficients for four river basin segments: St. Lawrence middle (a), Nile Upper (b), Nile middle (c), Nile lower(d). Each panel pair shows two quantities.Upper sub-panel shows the sensitivity of hot drought severity to SM′ (δ_1, blue) with dashed lines showing Theil–Sen trends; background colour encodes the soil-hot drought coupling regime in each year. Lower sub-panel shows z-scored land–atmosphere pathway coefficients: sensitivity of evaporation to soil moisture (α_1), daily maximum temperature to evaporation (γ_1), and precipitation to evaporation (φ_1). Background shading indicates the LA feedback pathway in each year

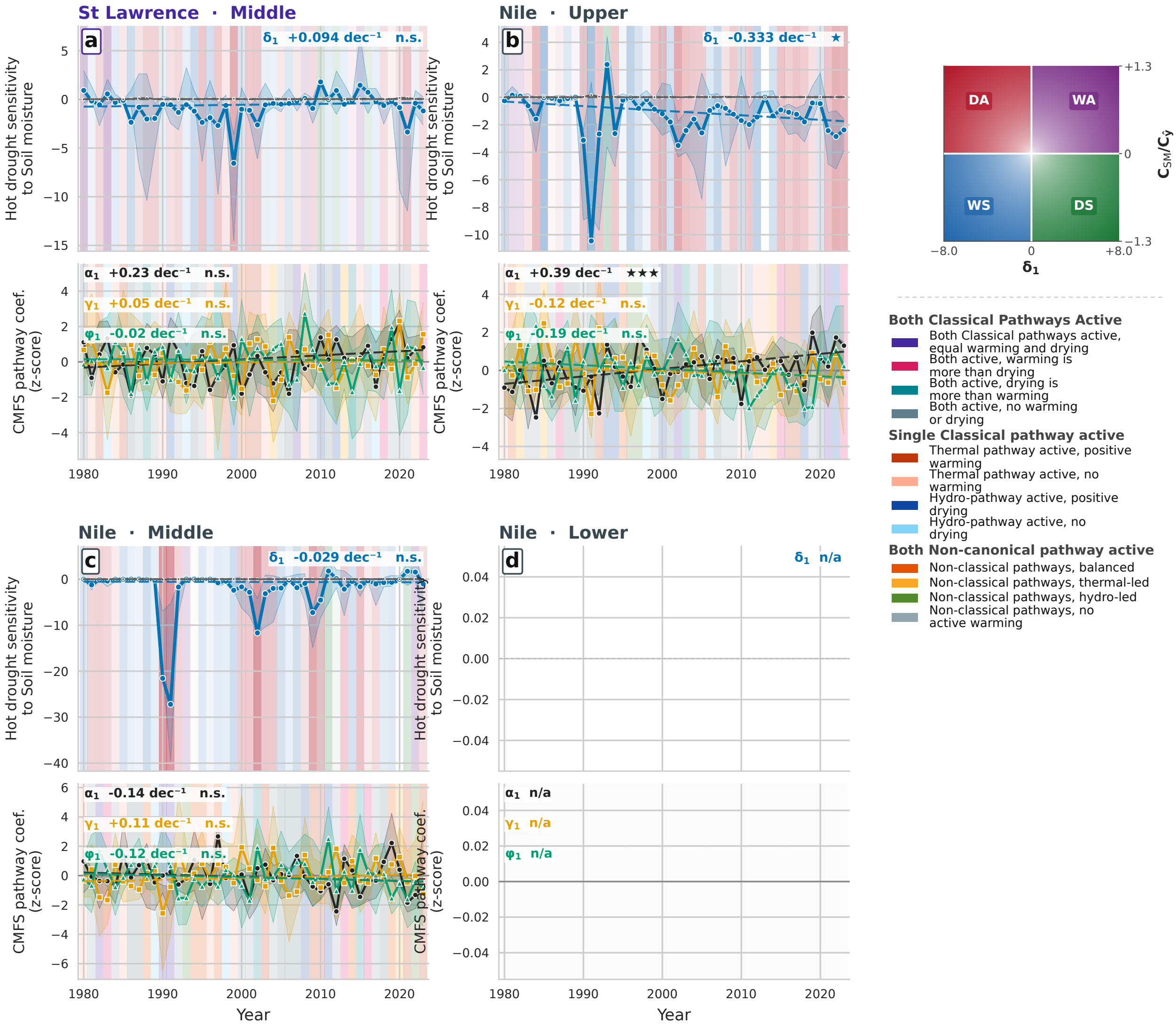

Supplementary Figure 12: (a–d) time series of soil-moisture-hot drought and land-atmospheric (CMFS) coupling coefficients for four river basin segments: St. Lawrence middle (a), Nile Upper (b), Nile middle (c), Nile lower(d). Each panel pair shows two quantities.Upper sub-panel shows the sensitivity of hot drought severity to SM′ (δ_1, blue) with dashed lines showing Theil–Sen trends; background colour encodes the soil-hot drought coupling regime in each year. Lower sub-panel shows z-scored land–atmosphere pathway coefficients: sensitivity of evaporation to soil moisture (α_1), daily maximum temperature to evaporation (γ_1), and precipitation to evaporation (φ_1). Background shading indicates the LA feedback pathway in each year

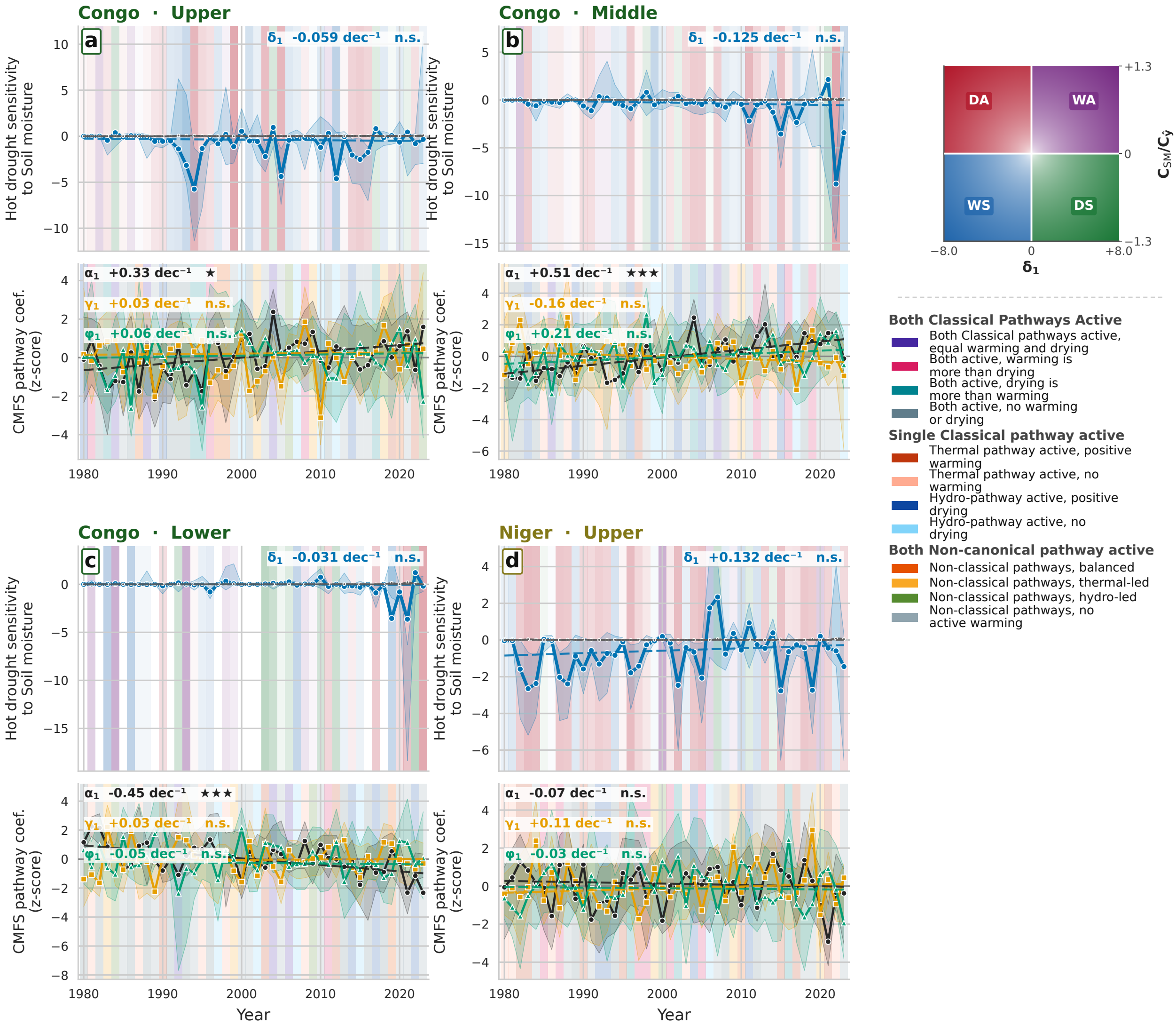

Supplementary Figure 13: (a–d) time series of soil-moisture-hot drought and land-atmospheric (CMFS) coupling coefficients for four river basin segments: Congo upper (a), Congo middle (b), Congo lower (c), Niger Upper(d). Each panel pair shows two quantities.Upper sub-panel shows the sensitivity of hot drought severity to SM′ (δ_1, blue) with dashed lines showing Theil–Sen trends; background colour encodes the soil-hot drought coupling regime in each year. Lower sub-panel shows z-scored land–atmosphere pathway coefficients: sensitivity of evaporation to soil moisture (α_1), daily maximum temperature to evaporation (γ_1), and precipitation to evaporation (φ_1). Background shading indicates the LA feedback pathway in each year

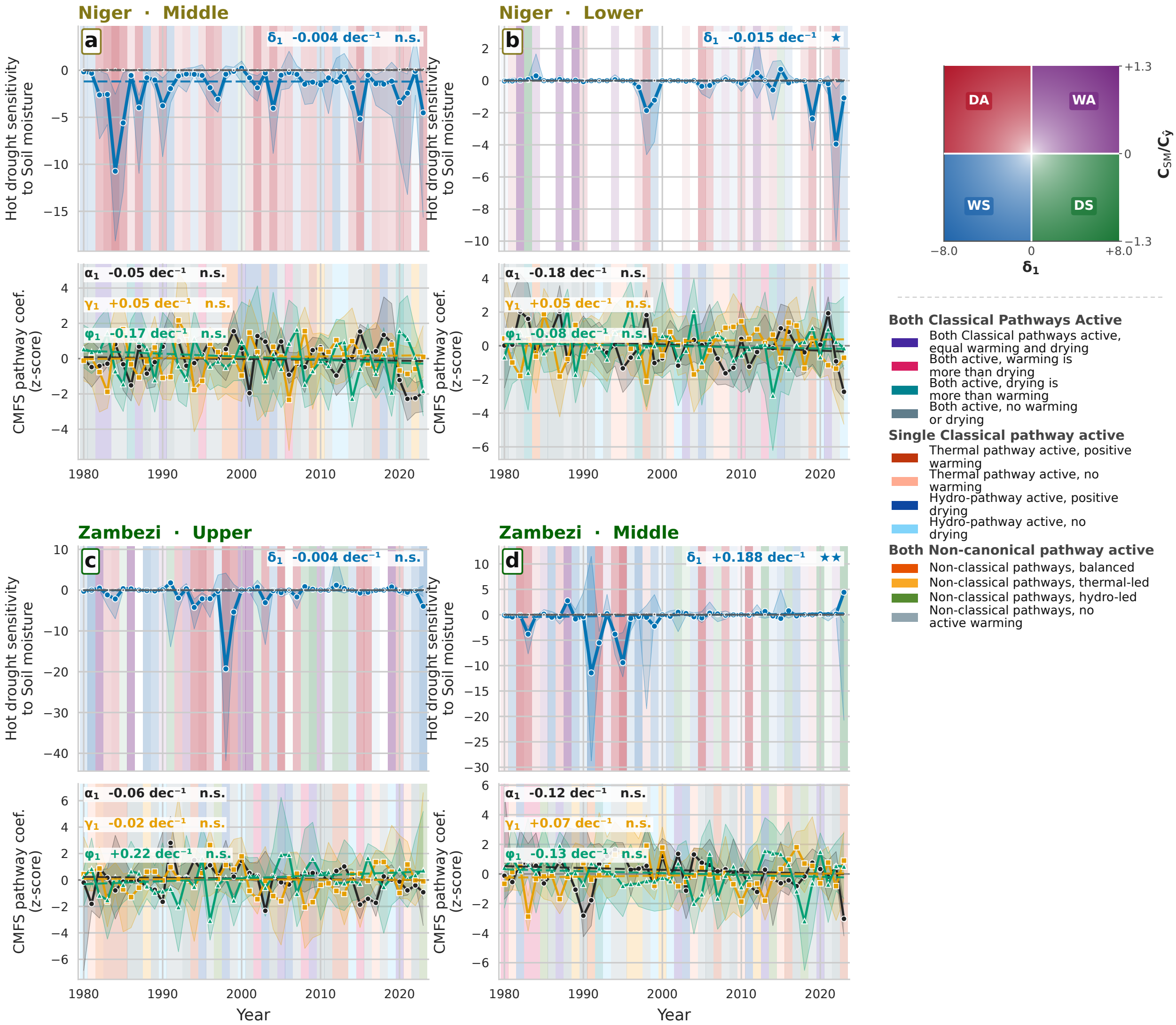

Supplementary Figure 14: (a–d) time series of soil-moisture-hot drought and land-atmospheric (CMFS) coupling coefficients for four river basin segments: Niger middle (a), Niger Lower (b), Zambeji upper (c), Zambeji middle(d). Each panel pair shows two quantities.Upper sub-panel shows the sensitivity of hot drought severity to SM′ (δ_1, blue) with dashed lines showing Theil–Sen trends; background colour encodes the soil-hot drought coupling regime in each year. Lower sub-panel shows z-scored land–atmosphere pathway coefficients: sensitivity of evaporation to soil moisture (α_1), daily maximum temperature to evaporation (γ_1), and precipitation to evaporation (φ_1). Background shading indicates the LA feedback pathway in each year

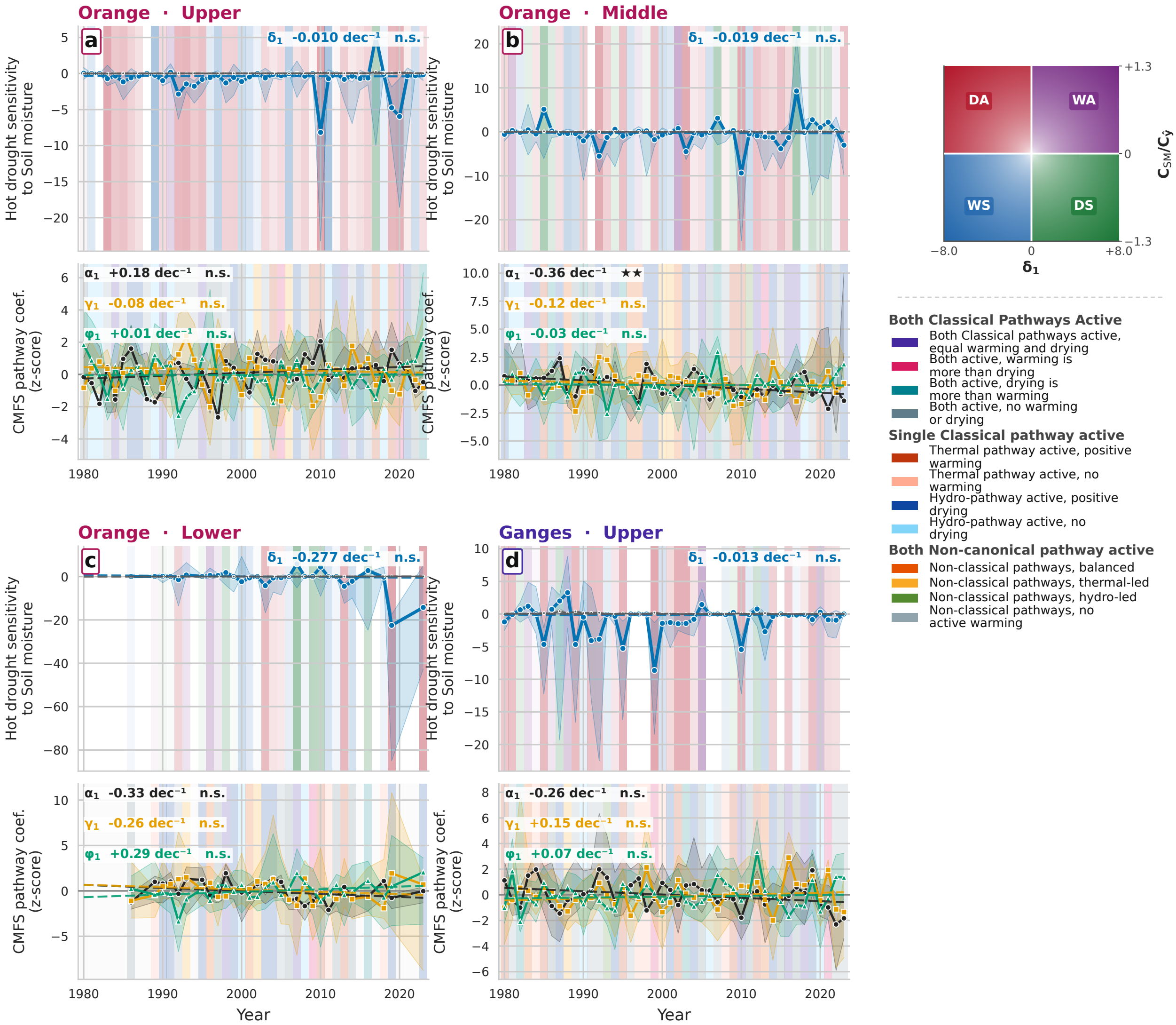

Supplementary Figure 15: (a–d) time series of soil-moisture-hot drought and land-atmospheric (CMFS) coupling coefficients for four river basin segments: Orange upper (a), Orange middle (b), Orange lower (c), Ganges upper(d). Each panel pair shows two quantities.Upper sub-panel shows the sensitivity of hot drought severity to SM′ (δ_1, blue) with dashed lines showing Theil–Sen trends; background colour encodes the soil-hot drought coupling regime in each year. Lower sub-panel shows z-scored land–atmosphere pathway coefficients: sensitivity of evaporation to soil moisture (α_1), daily maximum temperature to evaporation (γ_1), and precipitation to evaporation (φ_1). Background shading indicates the LA feedback pathway in each year

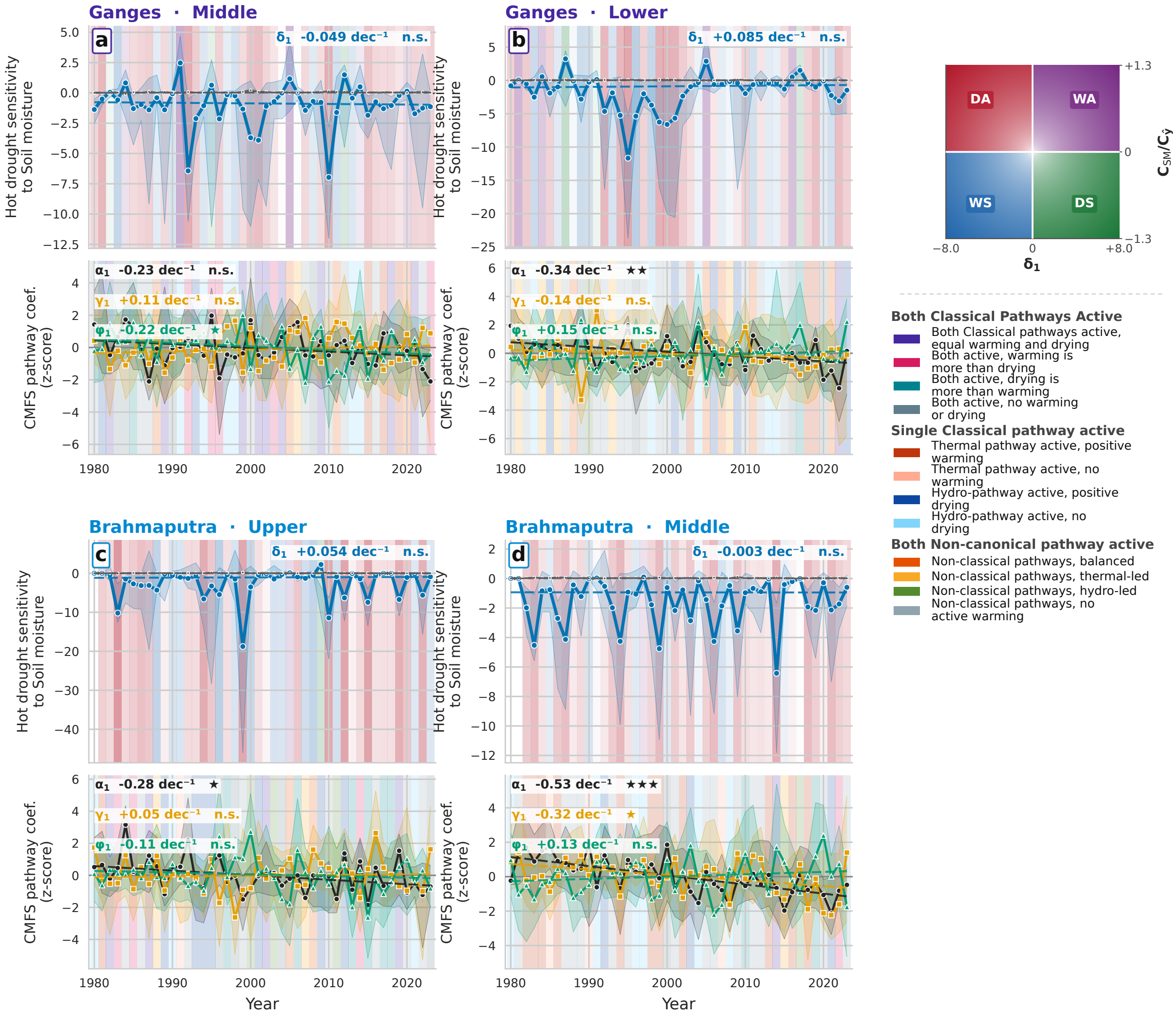

Supplementary Figure 16: (a–d) time series of soil-moisture-hot drought and land-atmospheric (CMFS) coupling coefficients for four river basin segments: Ganges middle (a), Ganges Lower (b), Brahmaputra upper (c), Brahmaputra middle (d). Each panel pair shows two quantities.Upper sub-panel shows the sensitivity of hot drought severity to SM′ (δ_1, blue) with dashed lines showing Theil–Sen trends; background colour encodes the soil-hot drought coupling regime in each year. Lower sub-panel shows z-scored land–atmosphere pathway coefficients: sensitivity of evaporation to soil moisture (α_1), daily maximum temperature to evaporation (γ_1), and precipitation to evaporation (φ_1). Background shading indicates the LA feedback pathway in each year

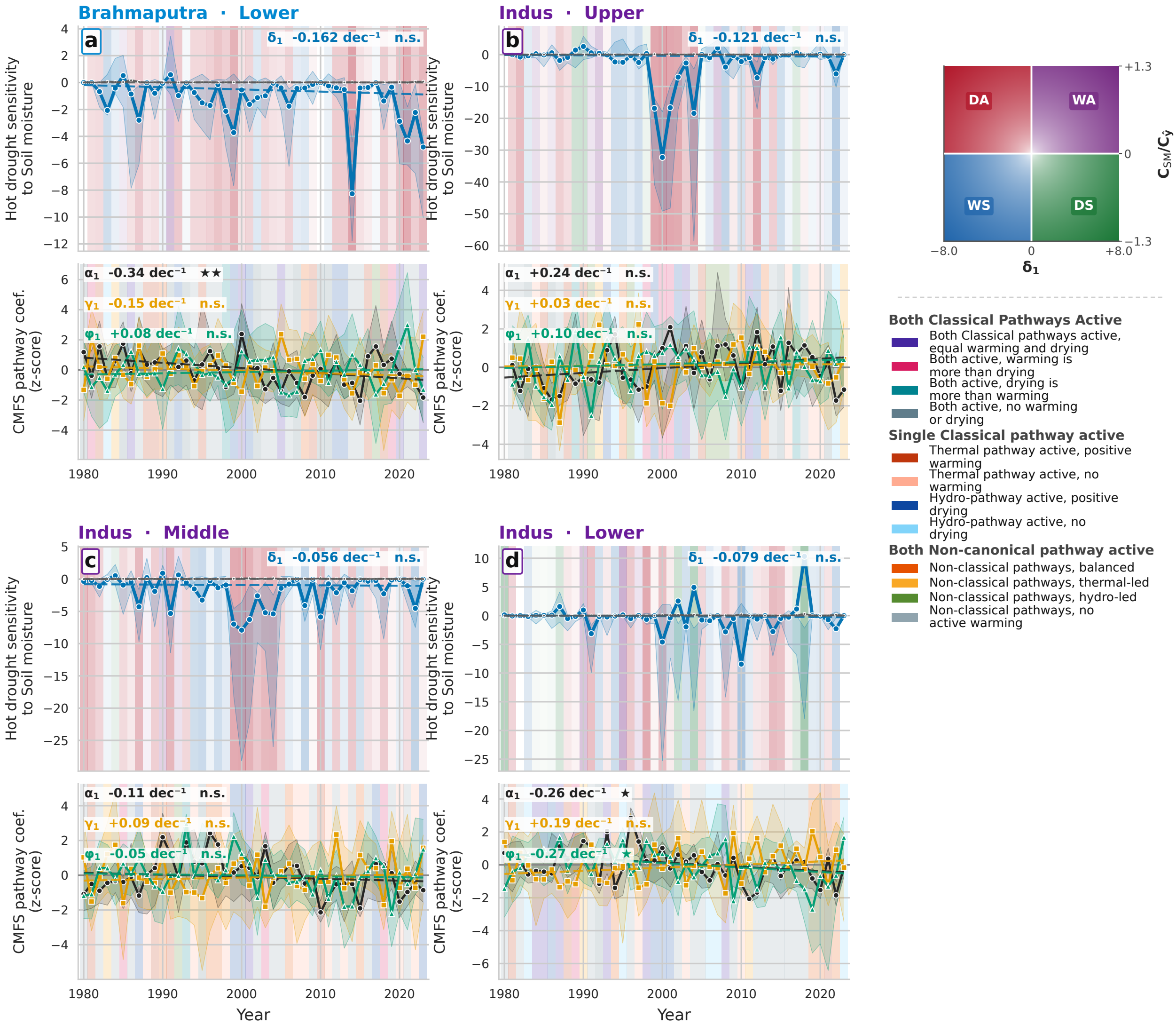

Supplementary Figure 17: (a–d) time series of soil-moisture-hot drought and land-atmospheric (CMFS) coupling coefficients for four river basin segments: Brahmaputra lower (a), Indus upper (b), Indus middle (c), Indus lower (d). Each panel pair shows two quantities.Upper sub-panel shows the sensitivity of hot drought severity to SM′ (δ_1, blue) with dashed lines showing Theil–Sen trends; background colour encodes the soil-hot drought coupling regime in each year. Lower sub-panel shows z-scored land–atmosphere pathway coefficients: sensitivity of evaporation to soil moisture (α_1), daily maximum temperature to evaporation (γ_1), and precipitation to evaporation (φ_1). Background shading indicates the LA feedback pathway in each year

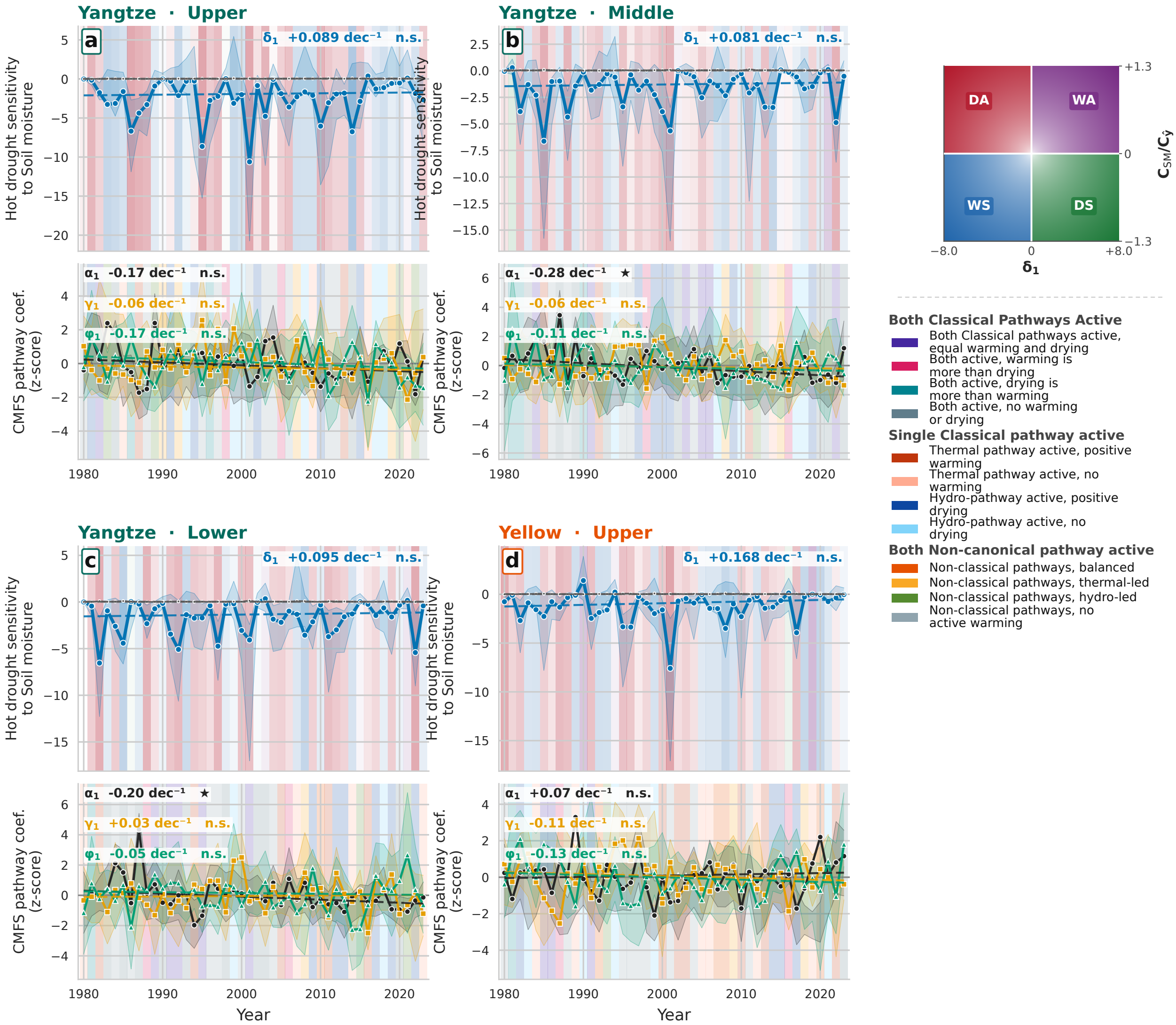

Supplementary Figure 18: (a–d) time series of soil-moisture-hot drought and land-atmospheric (CMFS) coupling coefficients for four river basin segments: Yangtze upper (a), Yangtze middle (b), Yangtze lower (c), Yellow upper(d). Each panel pair shows two quantities.Upper sub-panel shows the sensitivity of hot drought severity to SM′ (δ_1, blue) with dashed lines showing Theil–Sen trends; background colour encodes the soil-hot drought coupling regime in each year. Lower sub-panel shows z-scored land–atmosphere pathway coefficients: sensitivity of evaporation to soil moisture (α_1), daily maximum temperature to evaporation (γ_1), and precipitation to evaporation (φ_1). Background shading indicates the LA feedback pathway in each year

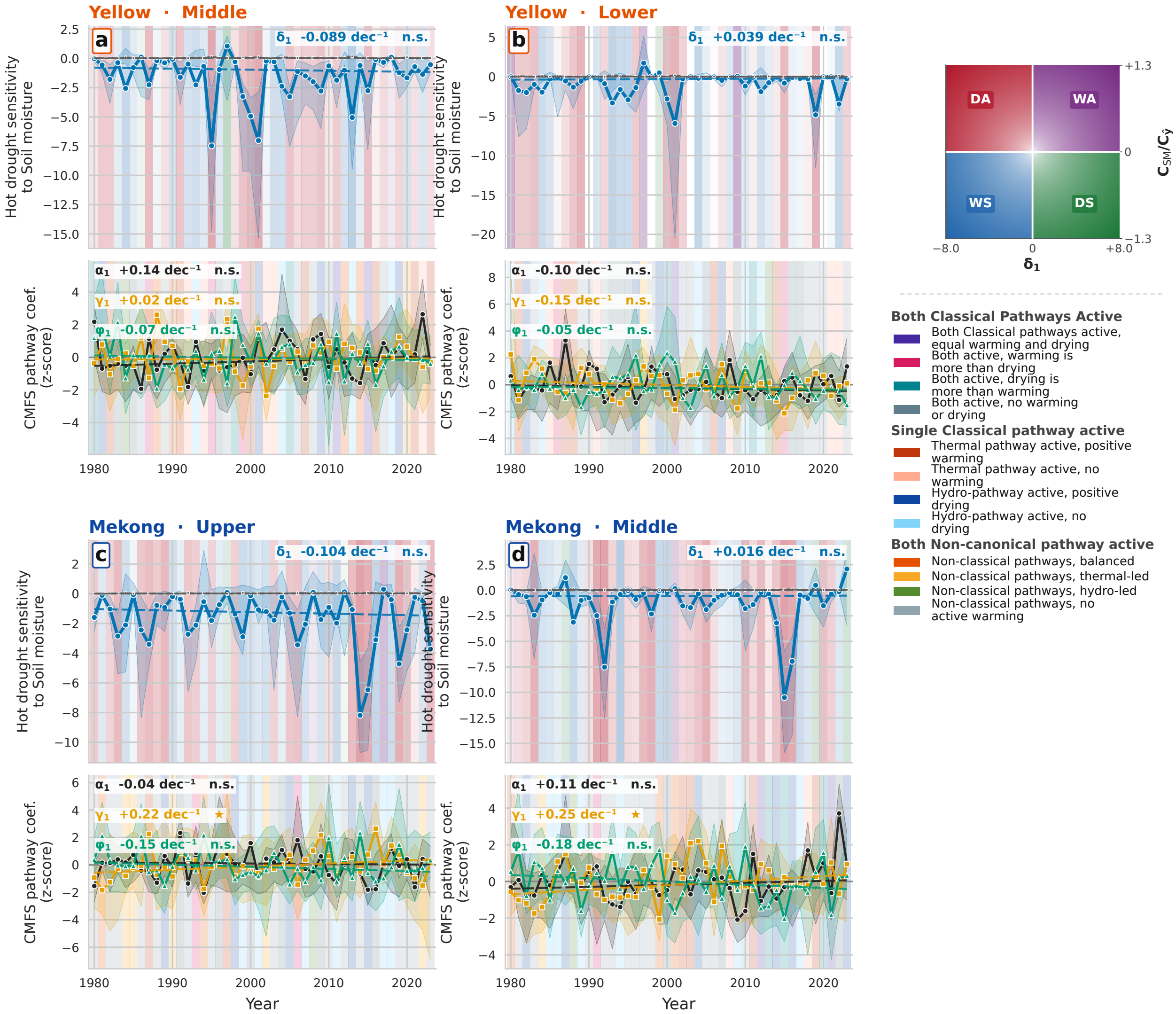

Supplementary Figure 19: (a–d) time series of soil-moisture-hot drought and land-atmospheric (CMFS) coupling coefficients for four river basin segments: Yellow middle (a), Yellow lower (b), Mekong upper (c), Mekong middle(d). Each panel pair shows two quantities.Upper sub-panel shows the sensitivity of hot drought severity to SM′ (δ_1, blue) with dashed lines showing Theil–Sen trends; background colour encodes the soil-hot drought coupling regime in each year. Lower sub-panel shows z-scored land–atmosphere pathway coefficients: sensitivity of evaporation to soil moisture (α_1), daily maximum temperature to evaporation (γ_1), and precipitation to evaporation (φ_1). Background shading indicates the LA feedback pathway in each year

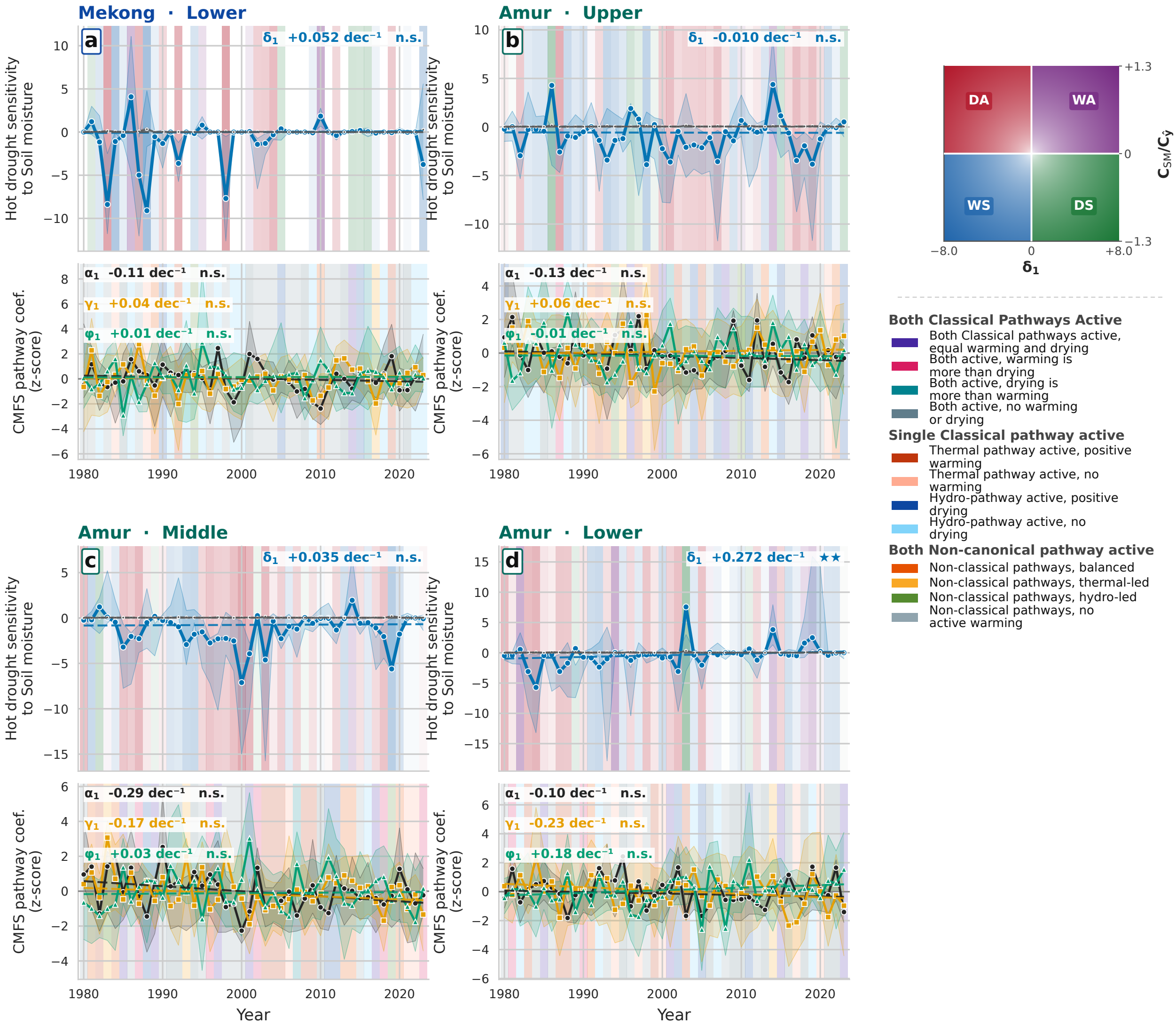

Supplementary Figure 20: (a–d) time series of soil-moisture-hot drought and land-atmospheric (CMFS) coupling coefficients for four river basin segments: Mekong lower (a), Amur upper (b), Amur middle (c), Amur lower(d). Each panel pair shows two quantities.Upper sub-panel shows the sensitivity of hot drought severity to SM′ (δ_1, blue) with dashed lines showing Theil–Sen trends; background colour encodes the soil-hot drought coupling regime in each year. Lower sub-panel shows z-scored land–atmosphere pathway coefficients: sensitivity of evaporation to soil moisture (α_1), daily maximum temperature to evaporation (γ_1), and precipitation to evaporation (φ_1). Background shading indicates the LA feedback pathway in each year

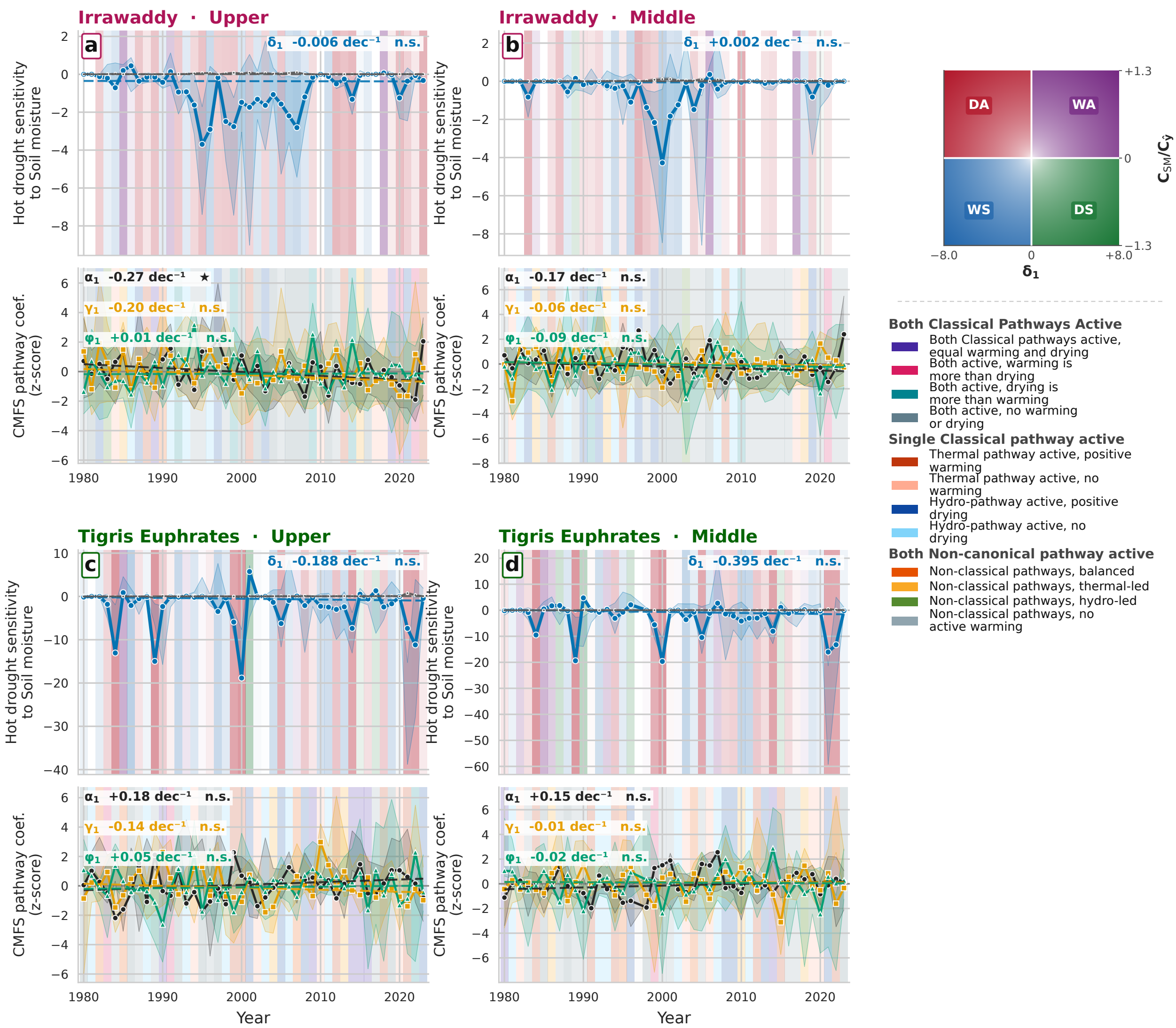

Supplementary Figure 21: (a–d) time series of soil-moisture-hot drought and land-atmospheric (CMFS) coupling coefficients for four river basin segments: Irrawaddy upper (a), Irrawaddy middle (b), Tigris Euphrates Upper(c), Tigris Euphrates Middle(d). Each panel pair shows two quantities.Upper sub-panel shows the sensitivity of hot drought severity to SM′ (δ_1, blue) with dashed lines showing Theil–Sen trends; background colour encodes the soil-hot drought coupling regime in each year. Lower sub-panel shows z-scored land–atmosphere pathway coefficients: sensitivity of evaporation to soil moisture (α_1), daily maximum temperature to evaporation (γ_1), and precipitation to evaporation (φ_1). Background shading indicates the LA feedback pathway in each year

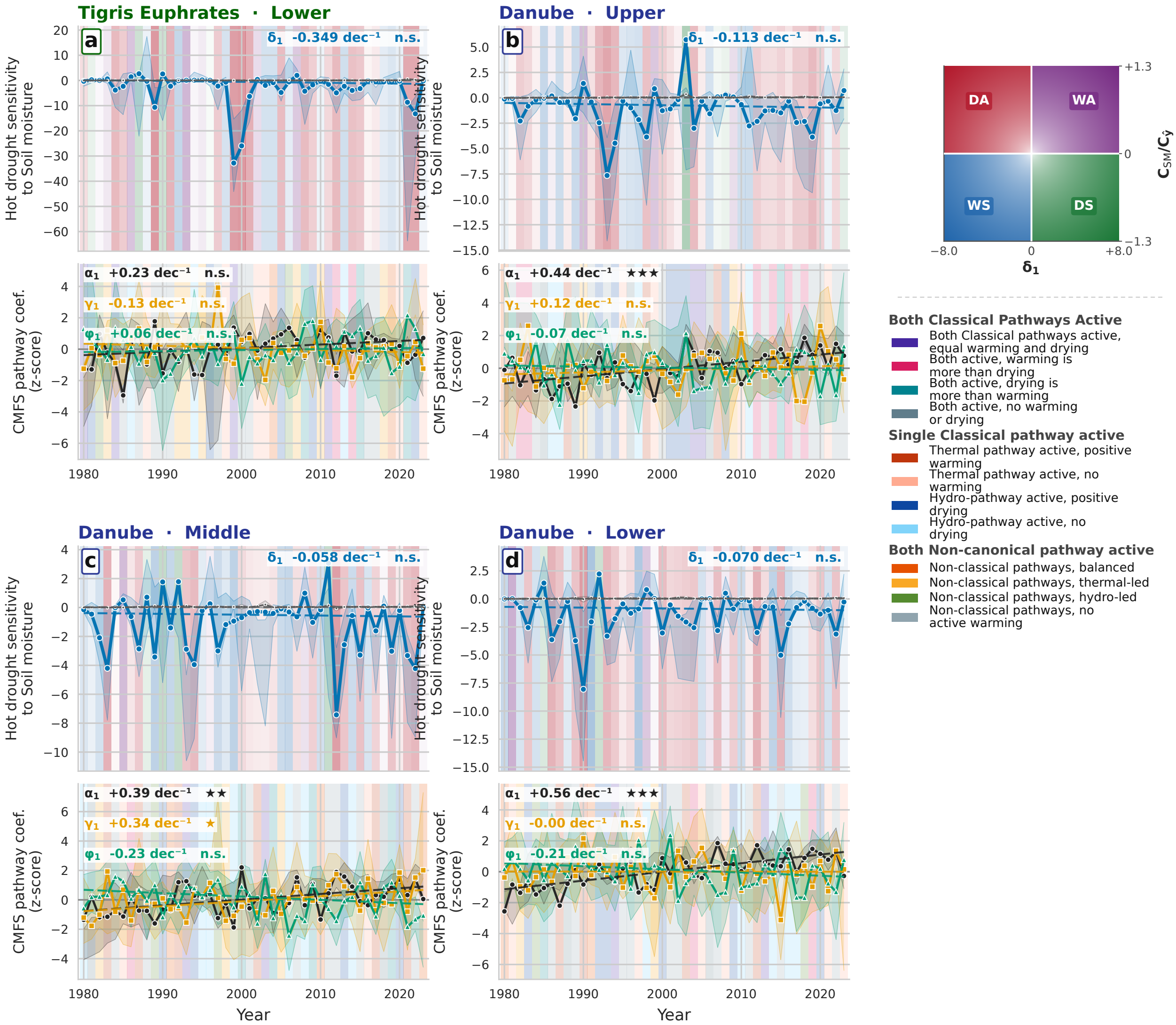

Supplementary Figure 22: (a–d) time series of soil-moisture-hot drought and land-atmospheric (CMFS) coupling coefficients for four river basin segments: Tigris and Euphrates lower (a), Danube upper (b), Danube middle (c), Danube lower(d). Each panel pair shows two quantities.Upper sub-panel shows the sensitivity of hot drought severity to SM′ (δ_1, blue) with dashed lines showing Theil–Sen trends; background colour encodes the soil-hot drought coupling regime in each year. Lower sub-panel shows z-scored land–atmosphere pathway coefficients: sensitivity of evaporation to soil moisture (α_1), daily maximum temperature to evaporation (γ_1), and precipitation to evaporation (φ_1). Background shading indicates the LA feedback pathway in each year

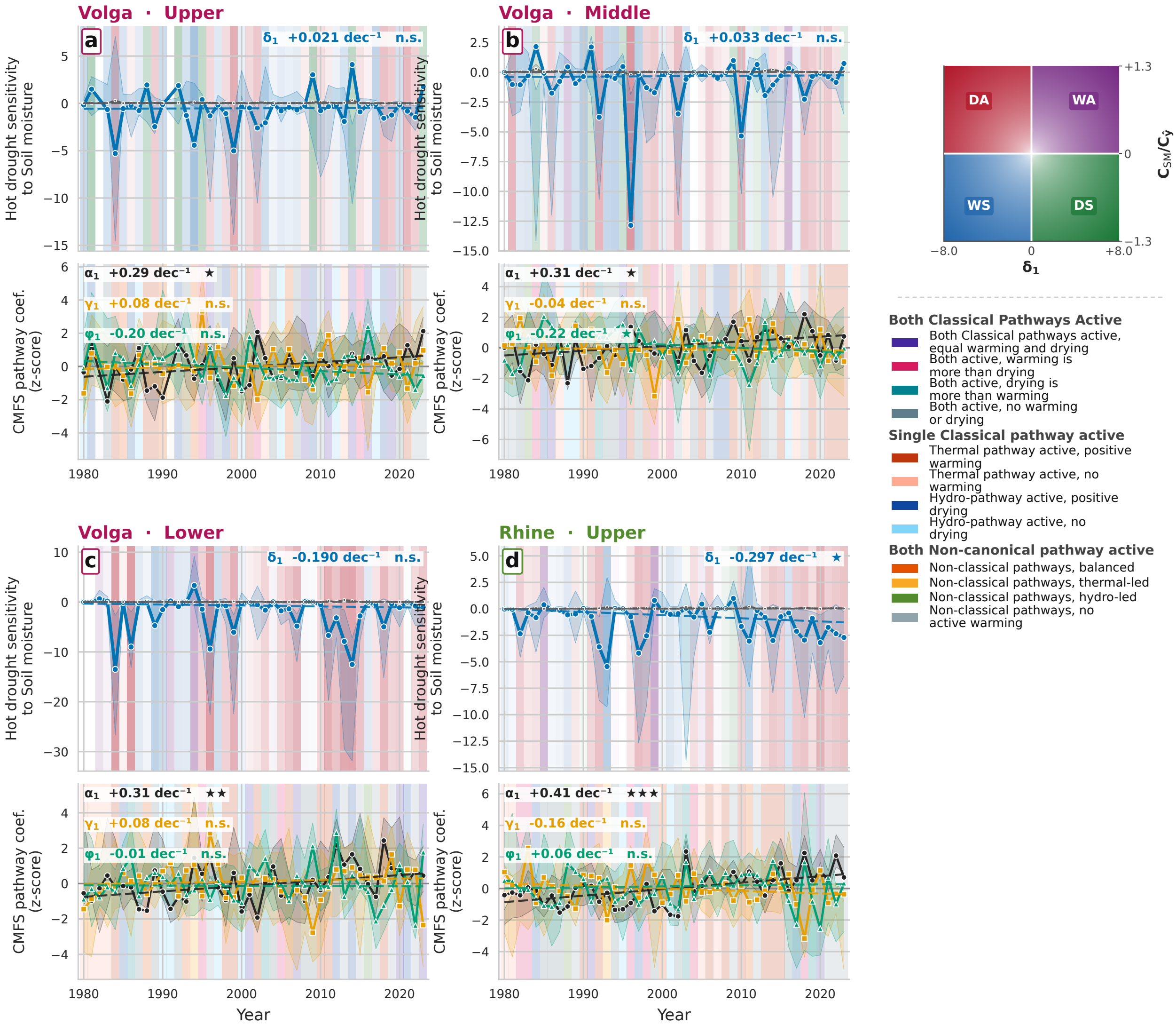

Supplementary Figure 23: (a–d) time series of soil-moisture-hot drought and land-atmospheric (CMFS) coupling coefficients for four river basin segments: Volga upper (a), Volga middle (b), Volga upper (c), Rhine upper (d). Each panel pair shows two quantities.Upper sub-panel shows the sensitivity of hot drought severity to SM′ (δ_1, blue) with dashed lines showing Theil–Sen trends; background colour encodes the soil-hot drought coupling regime in each year. Lower sub-panel shows z-scored land–atmosphere pathway coefficients: sensitivity of evaporation to soil moisture (α_1), daily maximum temperature to evaporation (γ_1), and precipitation to evaporation (φ_1). Background shading indicates the LA feedback pathway in each year

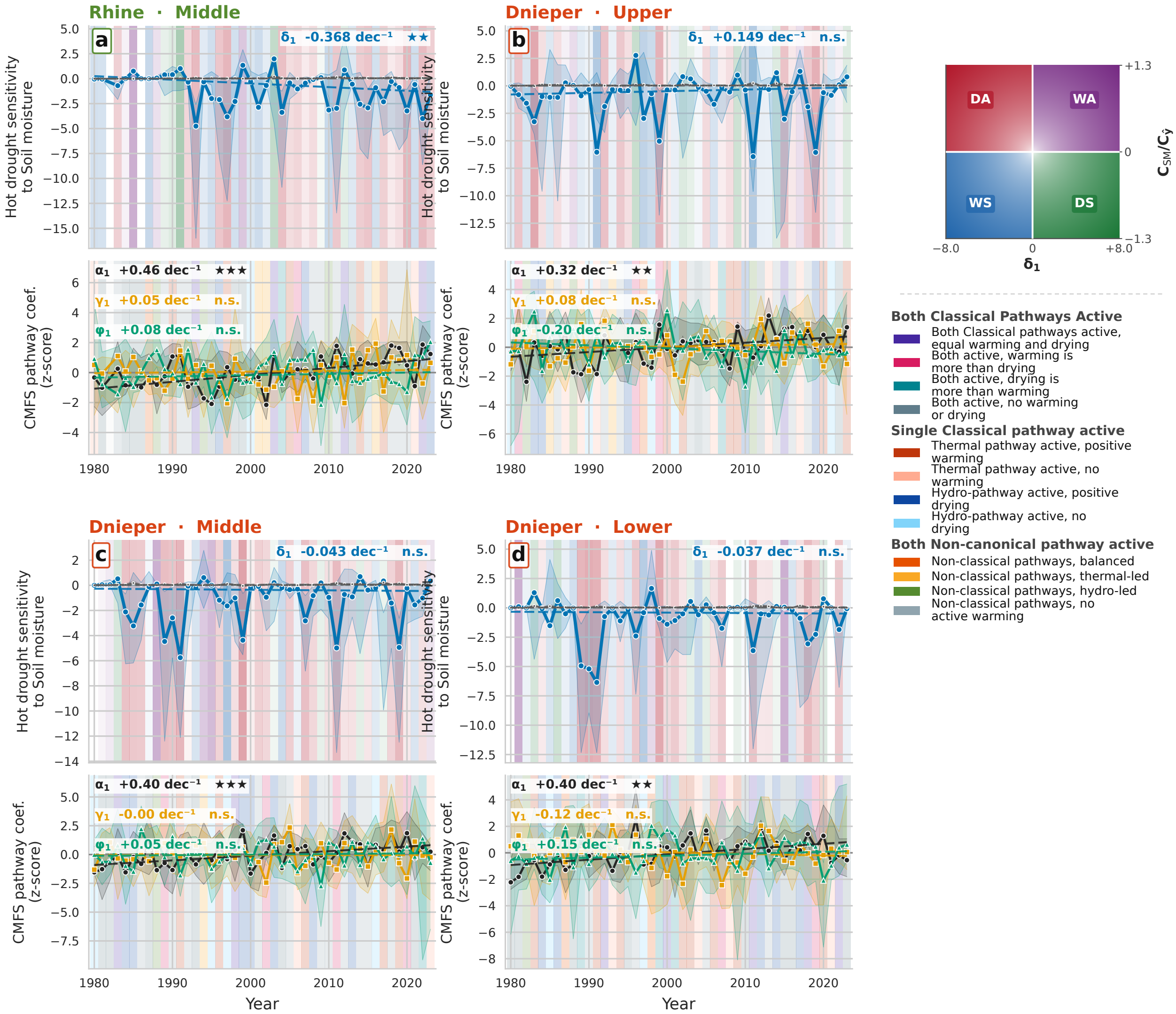

Supplementary Figure 24: (a–d) time series of soil-moisture-hot drought and land-atmospheric (CMFS) coupling coefficients for four river basin segments: Rhine middle (a), Dneiper upper (b), Deniper middle (c), Dneiper lower (d). Each panel pair shows two quantities.Upper sub-panel shows the sensitivity of hot drought severity to SM′ (δ_1, blue) with dashed lines showing Theil–Sen trends; background colour encodes the soil-hot drought coupling regime in each year. Lower sub-panel shows z-scored land–atmosphere pathway coefficients: sensitivity of evaporation to soil moisture (α_1), daily maximum temperature to evaporation (γ_1), and precipitation to evaporation (φ_1). Background shading indicates the LA feedback pathway in each year

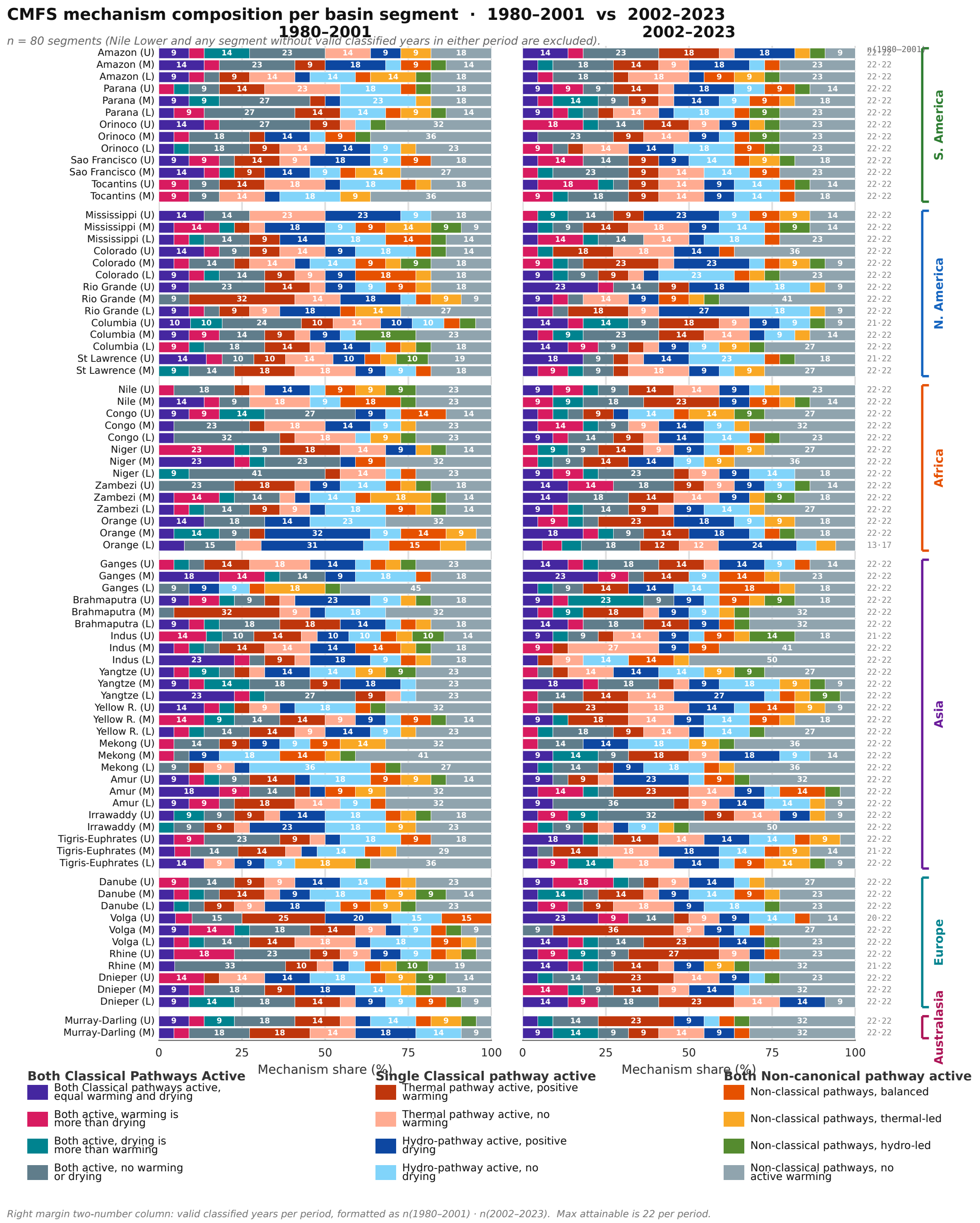

Supplementary Figure 25: Comparison of percentage distribution of land-atmospheric pathways between 2002-2023 with that of 1980-2001

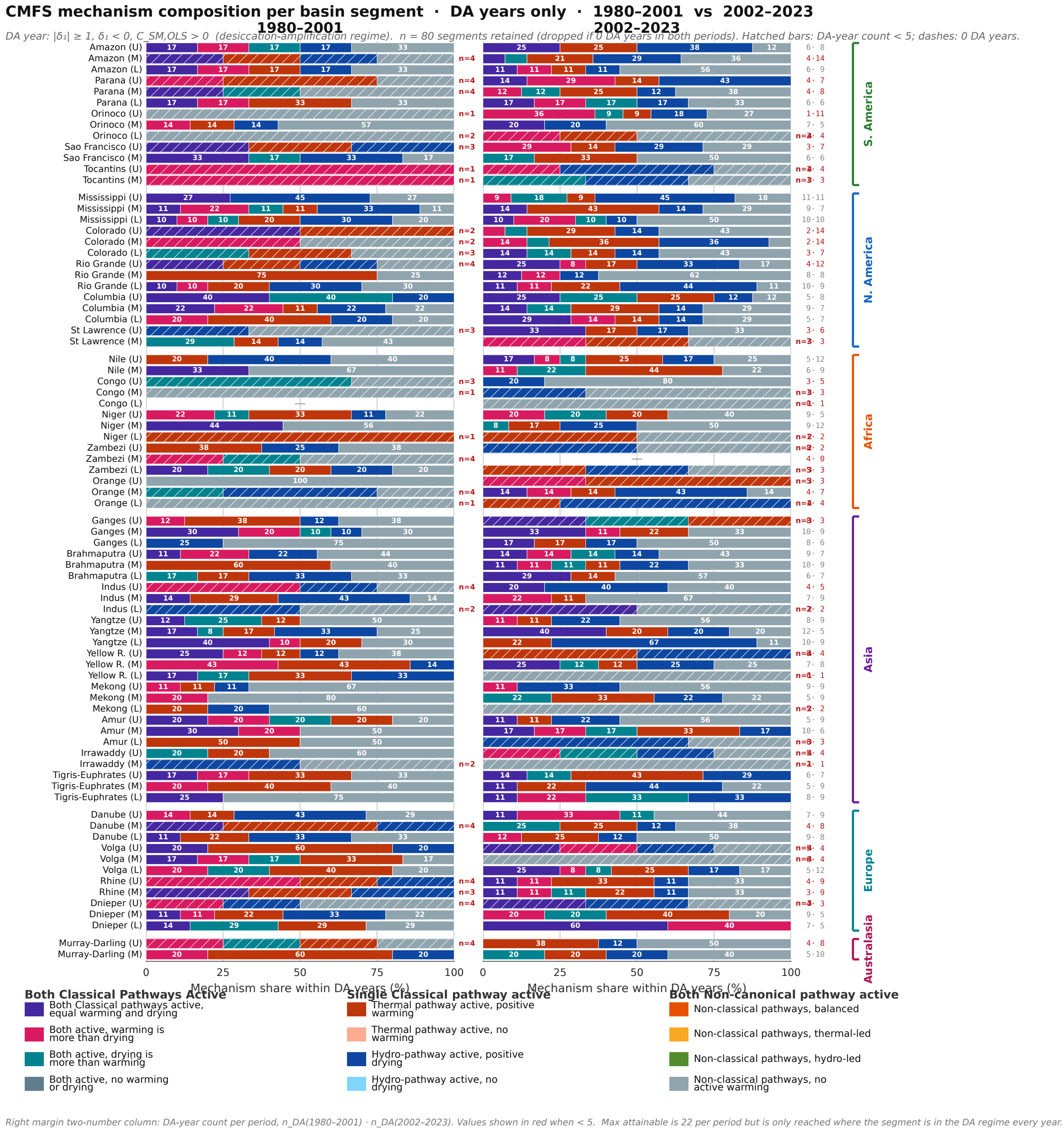

Supplementary Figure 26: Comparison of percentage distribution of land-atmospheric pathways in years when $SM - HD$ coupling is drying associated ampplification (DA) between 2002-2023 with that of 1980-2001

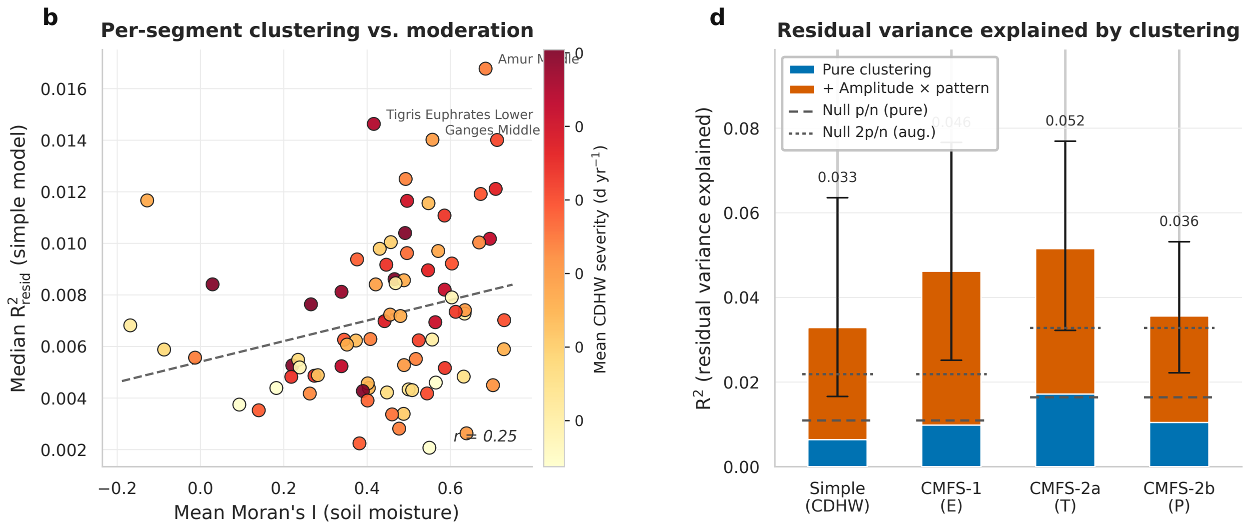

Supplementary Figure 27: (a) correlation between median moran's I and median residual from soil hot drought framework, (b) Amplitude augmented clustering model show higher regression than the null model indicating non-randomness

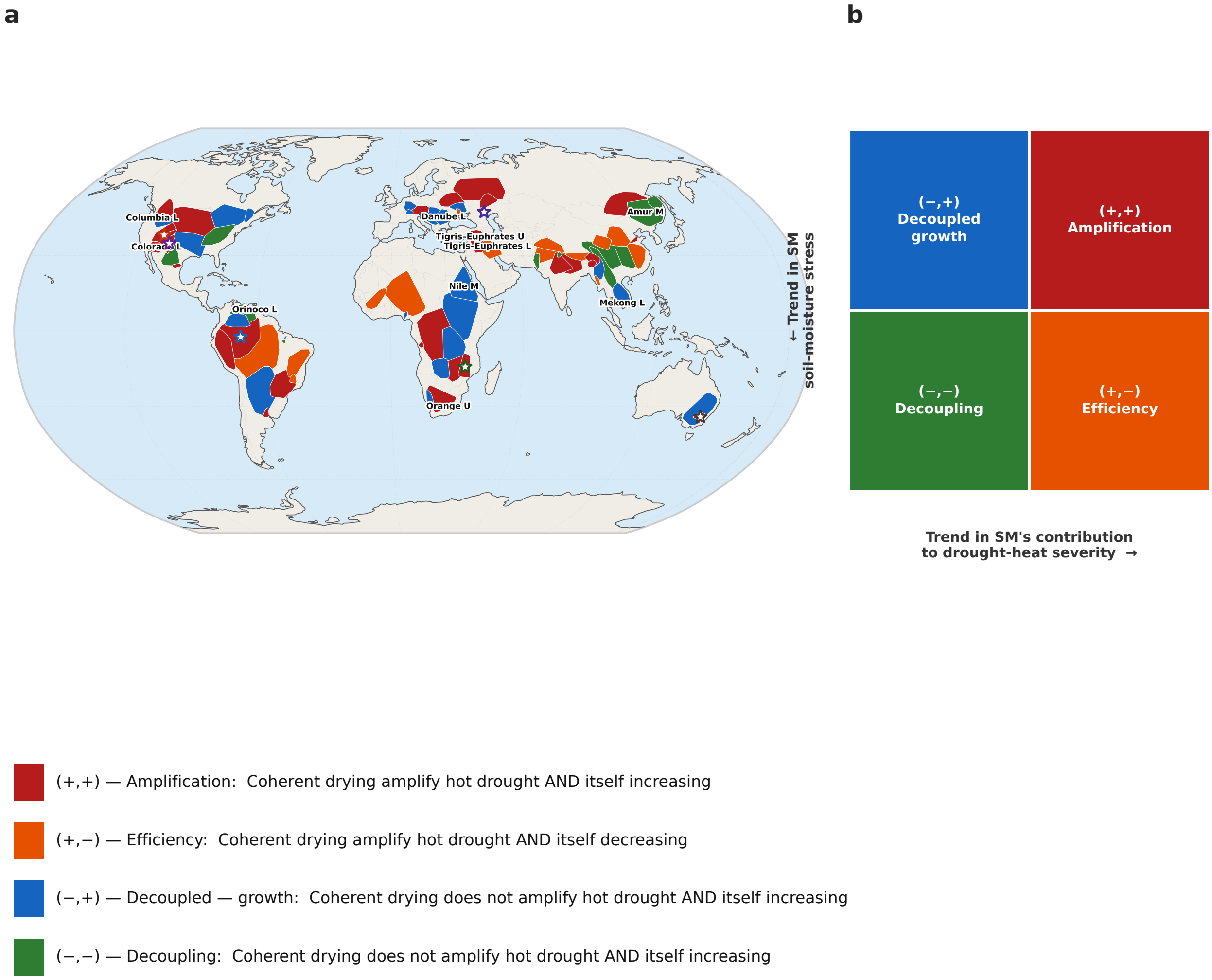

Supplementary Figure 28: (a) Trend in coherent drying and trend in how much coherent drying explains hot drought severity (b) The bivariate key showing the colors corresponding to different categories

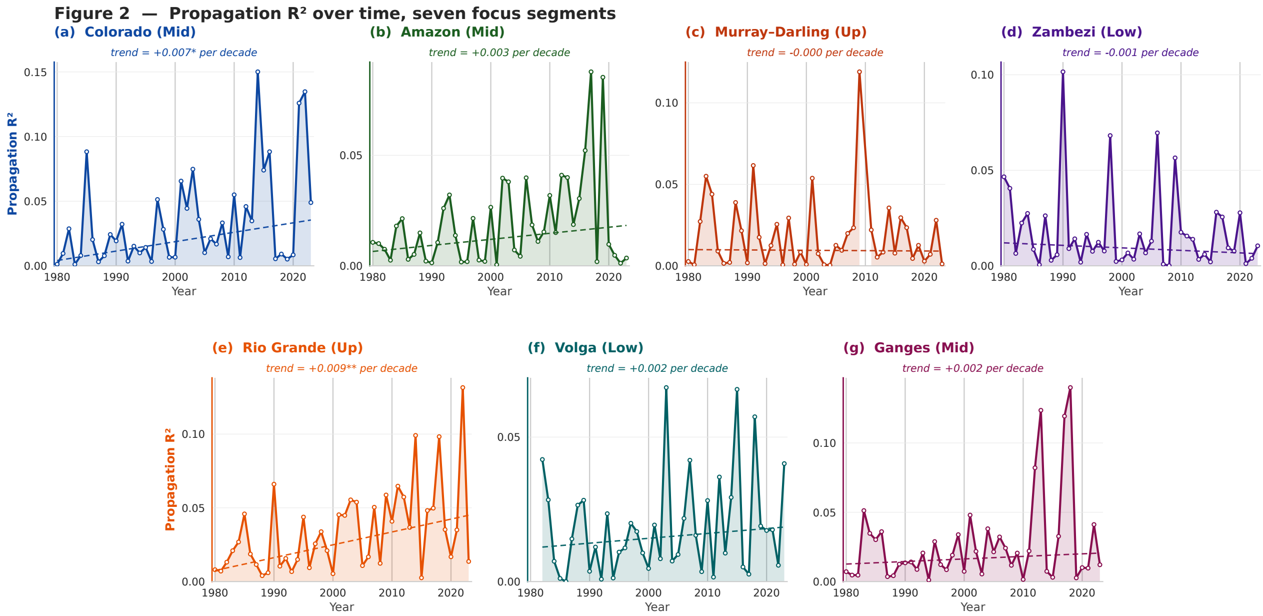

Supplementary Figure 29: Explainability of hot drought severity via remote proagation over(a) Colorado middle (b) Amazon middle, (c) Murray Darling upper, (d) Zambeji lower, (e) Rio grande upper, (f) Volga lower, (g) Ganges middle